Properties of Pt Electrodes Investigated by the Electrochemical Quartz Crystal Microbalance

by

Tao Wang
B.Sc., Tsinghua University, 2003

A Thesis Submitted in Partial Fulfillment of the
Requirements for the Degree of

MASTER OF SCIENCE

in the Department of Chemistry

University of Victoria

Properties of Pt Electrodes Investigated by the Electrochemical Quartz Crystal Microbalance

by

Tao Wang
B.Sc., Tsinghua University, 2003

Supervisory Committee

Dr. David A. Harrington, Supervisor
(Department of Chemistry)

Dr. Matthew Moffitt, Departmental Member
(Department of Chemistry)

Dr. Frank van Veggel, Departmental Member
(Department of Chemistry)

Dr. David Sinton, Outside Member
(Department of Mechanical Engineering)

Supervisory Committee

Dr. David A. Harrington, Supervisor
(Department of Chemistry)

Dr. Matthew Moffitt, Departmental Member
(Department of Chemistry)

Dr. Frank van Veggel, Departmental Member
(Department of Chemistry)

Dr. David Sinton, Outside Member
(Department of Mechanical Engineering)

Abstract

The Electrochemical Quartz Crystal Microbalance (EQCM) was used as the main investigation tool coupled with other conventional electrochemical methods to study the electrocatalytic properties of polycrystalline Pt electrodes, including two separate projects.

The first project studied the early stage of oxide film formation on the Pt surfaces and the inhibition of the catalytic properties by the oxide film. The inhibition of the fast electrode reaction of small molecules by the growth of oxide film allows those molecules to be used as probes for the nature of the oxide film. The hydrogen oxidation current (j_{ox}) calculated by differencing the cyclic voltammetry currents with and without H_2 present showed a characteristic plateau-to-plateau profile, which implies a transition from the free Pt surface to the Pt surface completely covered by oxide film. This method allows determination of the onset potential for oxide formation and also the critical potential where a full monolayer of oxide is formed. This method applies to other fast surface reactions such as oxygen reduction reaction (ORR), and the results are enhanced by forced convection in the rotating disk electrode (RDE) experiments. The initial oxidation species was identified by charge and EQCM frequency analysis. Our results support the formation of a species with stoichiometry Pt_2O, for example, with an oxygen atom in the bridging position between two adjacent Pt atoms.

In the second project, the stability of the Pt electrodes in acid media with Ag^+ present was investigated. A substantial frequency drift (8.3 Hz $cycle^{-1}$, or 44 ng cm^{-2} $cycle^{-1}$) was observed during Ag electrodeposition and stripping on the bare polycrystalline Pt surface. Cyclic voltammograms in pure $HClO_4$ solution showed nearly no frequency drift while the addition of 10^{-3} mol L^{-1} Ag^+ resulted in an immediate and characteristic frequency drift. The frequency drift appeared to be consistent with loss of material from the electrode surface and the ICP-MS detected a maximum Pt concentration of 2.3×10^{-6} mol L^{-1} in solution due to Pt dissolution. The Pt concentration calculated from the EQCM frequency drift matched the ICP-MS results. This allowed the EQCM for direct investigation of Pt dissolution at different system temperatures, sweep rates, and potential ranges. The much higher rate of dissolution with Ag present than that in pure $HClO_4$ solution can be explained by the formation of Pt-Ag alloy during Ag underpotential deposition and the co-dissolution of Pt and Ag.

Table of Contents

List of Tables

List of Figures

Nomenclature

Symbol	**Meaning**	**Units**
A_p	Piezoelectrically active area	cm^2
A_t	Electrochemically active area	cm^2
c_f	Differential calibration factor	$\mathrm{Hz\ ng}^{-1}$
$C*$	Bulk concentration	$\mathrm{mol\ L}^{-1}$
C_s	Surface concentration	$\mathrm{mol\ L}^{-1}$
C_f	EQCM calibration factor	$\mathrm{Hz\ ng}^{-1}\ \mathrm{cm}^2$
D	Diffusion coefficient	$\mathrm{cm}^2\ \mathrm{s}^{-1}$
E	Potential	V
E_a	Anodic potential limit	V
E_c	Cathodic potential limit	V
E_p	Peak potential	V
f	Frequency	Hz
f_0	Resonant frequency	Hz
F	Faraday's constant	$\mathrm{C\ mol}^{-1}$
j	Current density	$\mu\mathrm{A\ cm}^{-2}$
j_{H_2}	Current density with H_2 present	$\mu\mathrm{A\ cm}^{-2}$
j_{O_2}	Current density with O_2 present	$\mu\mathrm{A\ cm}^{-2}$
j_ox	Oxidation current density of H_2	$\mu\mathrm{A\ cm}^{-2}$
j_red	Reduction current density of O_2	$\mu\mathrm{A\ cm}^{-2}$
j_L	Limiting current density	$\mu\mathrm{A\ cm}^{-2}$
k	Rate constant	various

Symbol	**Meaning**	**Units**
m	Mass	g
M_e	Molar mass per electron	g mol^{-1}
t	Time	s
T	Temperature	°C
R^2	Goodness of fit	1
v	Sweep rate	mV s^{-1}
δ	Decay length	nm
η	Viscosity	Pa s
θ	Surface coverage	1
μ	Shear modulus	g cm^{-1} s^{-2}
ν	Kinetic viscosity	cm^2 s^{-1}
ρ	Density	g cm^{-3}
σ	Charge density	μC cm^{-2}
ω	Rotation rate	rad s^{-1}

Abbreviation	**Meaning**
AFM	Atomic force microscopy
CE	Counter electrode
CV	Cyclic voltammetry/voltammogram
HOR	Hydrogen oxidation reaction
ICP-MS	Inductively coupled plasma mass spectrometry
LEED	Low energy electron diffraction
ML	Monolayer
OPD	Overpotential deposition
ORR	Oxygen reduction reaction
QCM, EQCM	(Electrochemical) Quartz crystal microbalance
RDE	Rotating disk electrode
RRDE	Rotating ring disk electrode
RE	Reference electrode
RHE	Reversible hydrogen electrode
STM	Scanning tunneling microscopy
UPD	Underpotential deposition
WE	Working electrode

Acknowledgements

First I'd like to give many thanks and appreciation to my supervisor Dr. David Harrington. His careful and professional guidance to my research made my academic life in UVic a great achievement and enjoyment. His exceptional talents and passion in electrochemistry and mathematics impressed me a lot, and I learned to solve experimental problems from a fundamental perspective, usually starting from writing a kinetic equation for an electron transfer reaction. I also enjoyed total freedom to explore supplementary research subjects without worrying about deviating from my master thesis, travel around the world at my chosen times, and ask him all sorts of beginner's questions. Since my undergraduate years, I've been struggling over and over again to find a dream career which I will devote my life into. Now, I am happy to start as an electrochemist and for this David played the most important role.

I would like to thank my lab mates who accompanied and helped me along the way: Jakub Drnec, Bettina Roesch, Narissara Bussayajarn, Amanda Finn and Manuel Maréchal.

I give special thanks to my two supervisors Dr. Ping He and Dr. Siyu Ye in Ballard Power Systems where I did my 9-month coop work term. They were great mentors in helping me shaping my career profile, and I look forward to a chance to go back and work with them again.

Thanks to my committee member Prof. Frank van Veggel for his offering me the free usage of his AFM apparatus, and to Rob Cheyne in Prof. Matthew Moffitt's group for his training on the AFM. Thanks to Dr. Jody Spence in the School of Earth and Ocean Sciences for prompt help in providing the ICP-MS test results.

Thanks to the faculty and staff in the Chemistry department.

Lastly I thank the National Sciences and Engineering Research Council (NSERC) and the University of Victoria for funding my research.

To my dear Father and Mother.

Chapter 1

Introduction

The quartz crystal microbalance (QCM), more accurately referred to as the thickness-shear-mode (TSM) resonator, was developed to take advantage of the unique piezoelectricity of quartz crystals. These devices employ a thin quartz crystal sandwiched between two excitation electrodes, which exert an alternating electric field to drive the bulk crystal into synchronized vibration at its resonant frequency. The vibrating quartz senses a mass change on its electrode surfaces as a change in its natural resonant frequency. The mass change can be quantitatively estimated from this frequency shift, according to the pioneering work by Sauerbrey [1]. Accompanied with advanced frequency counting electronics, the QCM is able to measure minute mass changes at the nanogram level or less. For a long time the QCM was used almost exclusively in vacuum systems for film thickness detection as an supplementary component.

Advances in modern electrochemistry require detailed understanding of interfacial properties where electrochemical processes take place. Conventional electrochemical methods such as cyclic voltammetry (CV), chronoamperometry and chronopotentiometry have long been practiced for surface and thin film characterization. These methods, based on current and potential measurements, are able to provide kinetic and thermodynamic information for reactions, but have limited ability to elucidate compositional change and mechanism of film formation at surfaces. The QCM in solution for in situ mass measurement simultaneously with electrochemical measurements (one excitation electrode serves as the working electrode), is referred to as the electrochemical quartz crystal microbalance (EQCM), and is an established technique to aid in mechanistic studies of chemical or electrochemical processes at surfaces. The introduction of QCM into solution suffers immediately from heavy damping by liquid contact, and the initial applications were limited only to viscosity measurements. Subsequent theoretical effort was made by Bruckenstein [2] and Kanazawa [3] to clarify the liquid loading effect on mass detection. Since then, a proliferation in applications has been found in areas such as thin film deposition, adsorption, chemical sensors and biosensors. Today the EQCM is recognized as a powerful electroanalytical method in in-situ mass detection and interfacial property investigation.

The Pt surface, either single- or poly-crystalline, has been studied by many researchers extensively in the last five decades, due to its unique thermodynamic stability and catalytic properties for electrochemical reactions. A few excellent review articles are available in this area [4–6]. It is known that the properties of Pt surfaces can change dramatically when the surface condition is altered by oxidation, dissolution, passivation, surface alloy formation, etc.. This thesis examines the polycrystalline Pt surface under controlled modification, either by Ag electrodeposition or potential-induced oxidation, with the EQCM as the main investigation tool. The work presented in this thesis explores the potential of the EQCM technique to elucidate the mechanism of these surface processes, aiming for fundamental understanding of the properties of Pt surfaces under a variety of conditions, and their role as electrocatalysts. The outline of the rest of this thesis is as follows:

Chapter 2 discusses the experimental details.

Chapter 3 examines the non-ideal behavior of EQCM for in situ mass detection. This chapter gives background information about identifying variables that cause non-mass-related frequency components, and considerations for correct frequency interpretation. Some practical approaches to minimize the non-ideal effects are discussed.

Chapter 4 pertains to some recent advances in the continuing of interest in Pt oxide thin films and related areas in our research group. EQCM accompanied by platinum site blocking molecules (H_2 and O_2) is used to investigate the very initial stage of Pt oxide film formation. The initial composition and growth behavior are successfully identified.

Chapter 5 focuses on the interesting frequency drift phenomenon resulted from repeated Ag deposition and stripping. Direct in-situ proof by EQCM and Atomic force microscopy (AFM) is given of Pt dissolution from the electrode surface.

A short chapter 6 summarizing all my results and conclusions is placed at the end; it also addresses some future work to be done.

Chapter 2

Experimental

2.1 EQCM technique

2.1.1 Instrument set-up

Our current EQCM system integrates the frequency measurement with electrochemical capability. The electrochemical unit adopts a conventional 3-electrode cell design, using one excitation electrode on the quartz crystal surface as the working electrode (WE). The crystal is attached to the cell by a custom made Teflon holder (Fig. 2.1) with the WE side facing the solution and functions as the core part of the frequency measurement unit.

The 9 MHz AT-cut quartz crystal, purchased from Princeton Applied Research (PAR), has Pt disks (3000 Å thickness and 0.196 cm^2 geometric surface area) sputtered onto both of its sides, with a thin titanium adhesion layer underneath. The Pt surface has a polycrystalline structure and is available in a polished or unpolished version. In this work, we used crystals with the polished Pt surface, which has a true surface area of 0.235 cm^2, determined from the charge for H underpotential deposition (assuming one H per Pt atom corresponds to 220 $\mu C\ cm^{-2}$). The crystal

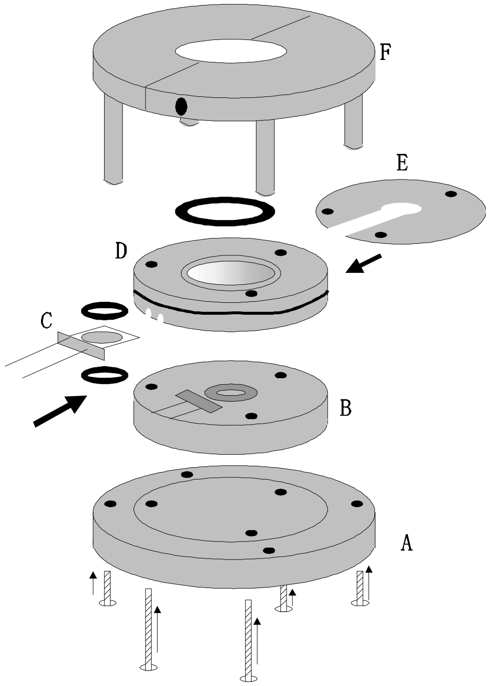

Figure 2.1: Schematic of EQCM Teflon holder. A) Bottom metal piece. B) Bottom Teflon piece. C) EQCM crystal between two o-rings. D) Top Teflon piece. E) Metal supporing piece. F) Metal unit attached to the glass cell. Reprinted with permission from Ref. [7]. Copyright C.A. Jeffrey, 2004 University of Victoria.

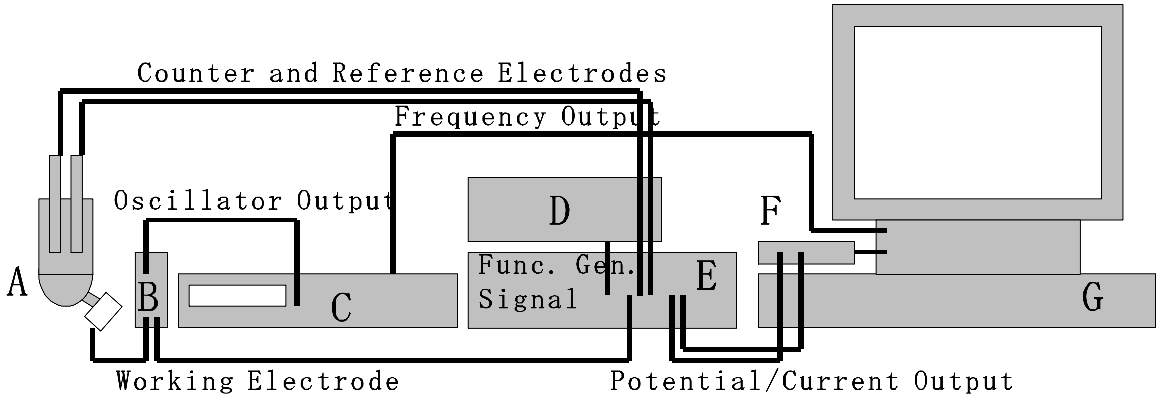

Figure 2.2: Schematic for the EQCM set up. A) Electrochemical and EQCM cell. B) Voltage-controlled oscillator. C) High-resolution frequency counter. D) Analog or digital function generator. E) Potentiostat. F) Picoscope analog-to-digital converter. E) Data acquisition computer. Reprinted with permission from Ref. [7]. Copyright C.A. Jeffrey, 2004 University of Victoria.

is sandwiched between o-rings in the teflon holder, and operated by a phase locked oscillator (Maxtek PLO-10i). The PLO-10i outputs the frequency signal to a high-resolution frequency counter (Fluke PM6681) and also connects the current signal from the WE to a custom-built potentiostat, which controls the potential. Analogue current and potential signals from the potentiostat are digitized with a 12-bit analog-to-digital converter (ADC-212, Pico Technologies) and collected together with the digital output of the frequency counter using custom software. To avoid electromagnetic interference, the quartz crystal and oscillator were placed in a Faraday cage. The detailed schematic of the EQCM set-up and data acquisition is presented in Fig. 2.2.

2.1.2 Electrochemistry

Solutions were prepared from analytical grade chemicals and Millipore Milli-Q deionized water: 0.5 M H_2SO_4 (BDH Aristar), 0.5 M $HClO_4$ (BDH), 1 mM $AgClO_4$ (Alfa Aesar) in 0.5 M $HClO_4$ (later simply referred to as 1 mM $AgClO_4$ in this thesis). The solution was deoxygenated by bubbling a constant argon (ACS grade) stream prior to and throughout any electrochemical measurement. For Chapter 4 where H_2 or O_2 saturated solution was needed, ultra high purity H_2 or O_2 gas was supplied directly from a high pressure tank, without special pretreatment, with the flow rate controlled by the regulator. A fine stream of 2-3 bubbles per second was maintained without causing apparent convection in solution.

The WE was the polycrystalline Pt electrode on the quartz crystal facing the solution, and either side could be used. For H_2SO_4 and $HClO_4$ solutions, the reversible hydrogen electrode (RHE) was used as a reference electrode, made of high purity poly-crystalline Pt wire sealed in glass tubes, isolated from the main cell solution with a luer ground glass joint wetted with electrolyte. For $AgClO_4$ solutions where the usage of the RHE is unworkable, $Ag|Ag^+$ reference electrodes (RE) were used, made of high purity Ag wire immersed in the main cell solution. The equilibrium potential of $Ag|Ag^+$ RE in 1 mM $AgClO_4$ was calculated to be 0.60 V versus RHE in 0.5 M $HClO_4$, and this correlation was used to convert potential measured versus one RE to that versus another. The counter electrode (CE) had a small Pt gauze welded to the Pt wire to provide sufficient surface area.

All the glassware, electrodes and teflon pieces were soaked in a hot chromic acid bath and then rinsed thoroughly with Millipore water. The quartz crystal was treated with Millipore Milli-Q water by long-time soaking and rinsing. Before any actual measurement, a few cyclic voltammetry (CV) cycles between 0.05 and 1.45 V at 20 mV s^{-1} were performed until the voltammogram included only the features of clean polycrystalline platinum (see Fig. 2.3). In Ag electrodeposition experiments, the 0.5 M $HClO_4$ solution was replaced by 1 mM $AgClO_4$ solution after the electrode was electrochemically cleaned. All CVs were operated between 0.05 V and 1.55 V vs. RHE, or 0.6 V and 0.9 V vs. $Ag|Ag^+$ in $AgClO_4$ solution if not otherwise specified, controlled by the potentiostat, with current densities quoted relative to the true area. The frequency response was recorded simultaneously when electrochemical

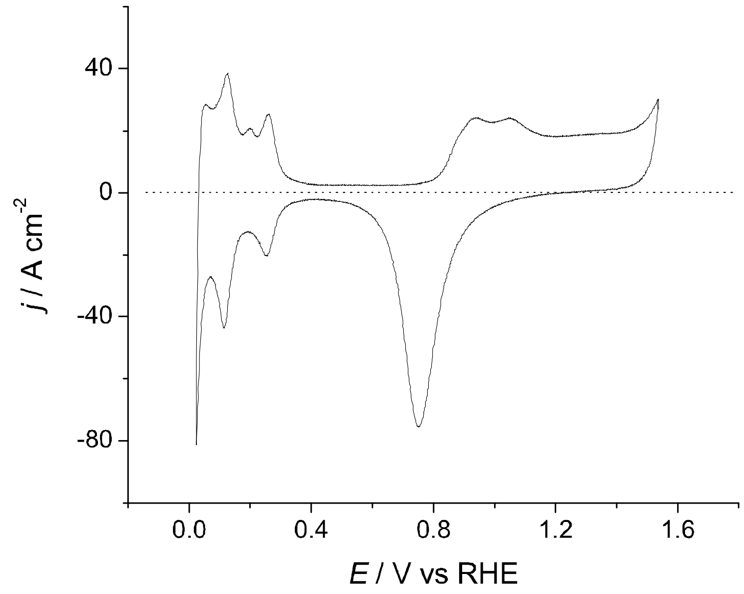

Figure 2.3: Cyclic voltammetry in 0.5 M H_2SO_4, sweep rate 20 mVs^{-1}, polycrystalline Pt electrode

experiments were conducted on the electrode. All the measurements were carried out at room temperature.

2.1.3 Frequency data treatment and analysis

The frequency counter adopts a reciprocal counting technique to measure the frequency, with theoretical resolution inversely proportional to gate time t_g. This gate time represents the time resolution in capturing the frequency change in a fast electrochemical process. To achieve fast frequency measurements with high resolution, the effect of t_g was carefully tested and a default value of 10 ms was chosen. The frequency data measured in $AgClO_4$ solutions had a high signal-to-noise ratio (S/N), due to the large frequency change (ca. 500 Hz) by deposition of heavy Ag atoms, and hence raw data was used for frequency analysis without smoothing. The electrode reaction in $HClO_4$ or H_2SO_4 involves only light species such as H and O, resulting in a small total frequency change (ca. 30 Hz) and poor S/N. In such cases, the raw frequency data was treated by a 30 point fast fourier transform (FFT) based smoothing technique to filter the noise while faithfully representing the signal (Fig. 2.4).

The relationship between mass change per unit EQCM surface area (Δm) and its corresponding frequency shift (Δf) in the natural resonant frequency was governed by the Sauerbrey equation,

$$\Delta f = -2f_0^2\Delta m/(\rho_{\mathrm{q}}\mu_{\mathrm{q}})^{1/2} \text{ or } \Delta f = C_{\mathrm{f}}\Delta m \tag{2.1}$$

where f_0 is the natural resonant frequency in air, ca. 9 MHz for our quartz, ρ_{q} is the density of quartz (2.648 g cm^{-3}), and μ_{q} is the shear modulus of quartz (2.947×10^{11} g cm^{-1} s^{-2}). These three constants are the intrinsic physical properties of a given piece of quartz crystal, and usually represented by a simple combined constant C_{f}, which not only quickly gives the mass change from the measured frequency, but also tells how sensitively the EQCM responds to mass change. The proportional relationship between frequency shift and mass change holds when the mass change is within 1% of the total quartz mass and this condition was easily met in our experiments. The actual C_{f} needs to be carefully calibrated, although a nominal one is available from theoretical calculation or the manufacturer. The common approach as suggested by many researchers is experimental calibration by electrodeposition of a heavy metal, such as copper or silver. In this work, C_{f} of 0.188 ± 0.004 Hz ng^{-1} cm^2 was determined with methods described in Ref. [8] by Ag electrodeposition and is used exclusively in this thesis. The errors in mass measurement were calculated from the standard deviations of serveral replicate experiments. With a confidence level of 95%, the errors are approximately 10% of the average mass.

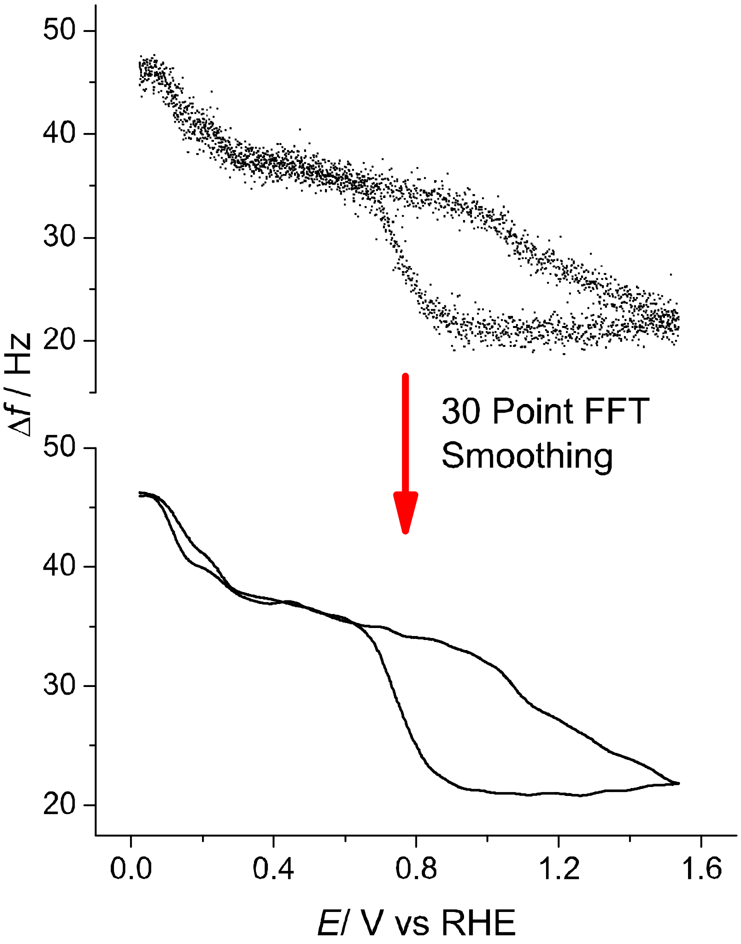

Figure 2.4: Example of FFT smoothing. Frequency data obtained under the same condition as Fig. 2.3.

2.2 Rotating disk electrode technique

The rotating disk electrode (RDE) is an important hydrodynamic method to study electrochemical processes involving convective mass transport. In cases where the current-potential feature is complicated by the natural convection in stagnant solution, the rotating electrode produces a controlled convection at much higher magnitude, so that the random convection can be effectively eliminated. The resulting current response becomes much higher due to the additional convective component, compared with diffusion controlled current in stagnant solution. The mathematical description of the limiting current j_{L} controlled by mass transport on a rotating disk at steady state has been given by Levich [9]:

$$j_{\mathrm{L}} = 0.620nFC^{*}D^{2/3}\nu^{-1/6}\omega^{1/2} \tag{2.2}$$

where n is the number of electrons for the overall reaction, F is Faraday's constant, C^{*} is the bulk concentration, D is the diffusion coefficient, ν is the kinematic viscosity and ω is the rotation speed in rad s^{-1}. Eq. (2.2) applies to a fast electron transfer reaction at totally mass-transport-limited condition. When the reaction is slower and limiting current condition can't be achieved, Eq. (2.2) needs to be modified into a general current-potential equation, including both kinetics and mass transport components:

$$\frac{1}{j} = \frac{1}{nFkC^{*}} + \frac{1}{0.620nFC^{*}D^{2/3}\nu^{-1/6}\omega^{1/2}} \tag{2.3}$$

where k denotes the rate constant of the charge transfer reaction.

We used the RDE technique in our studies of Pt oxide formation (Chapter 4) where significant convection was caused in solution by H_2 and O_2 bubbling. The experiment was carried out in a specially designed three-electrode glass cell to accommodate the rotating disk tip. The rotating disk tip (Pine instrument MT28 series) was a teflon rod with a Pt disk and Pt ring embedded in the end, with the disk and ring separated by a thin teflon gap. In Chapter 4, the Pt disk was used as the working electrode, and had a true surface area of 0.268 cm^2. The RDE tip was polished by a series of diamond compound pastes, with particle size from 300 μm to 1 μm and then rinsed thoroughly with Millipore water. The RDE was driven by a rotating Modulated Speed Rotator (MSR), with the rotating speed controlled over a wide range from 1 to 10000 rpm.

2.3 ICP-MS technique

Inductively Coupled Plasma Mass Spectrometry (ICP-MS) is an extremely sensitive analytical technique, capable of measuring multi-element concentrations in a given sample from ultra-trace (ppb) to major component levels (mM). Both liquid and solid (digested in aggressive acid mixture) samples can be analyzed.

The diluted sample is injected with argon gas, nebulized and then enters the plasma torch, which is the heat source and provides a high temperature at 8000 K to ionize the analyte completely. The ions are extracted from the plasma through sampling and skimmer cones, into a low vacuum region. The quadrupole will only let ions of a certain mass and charge pass through and into the detector. By this method most elements in the periodic table, from lithium to uranium, can be measured and quantified. A detailed schematic is given in Fig 2.5.

Detection of soluble Pt dissolved from the Pt electrode was carried out on a Thermo XSII X7 Quadrupole ICP-MS. Samples were handled and prepared in an ultra clean room. All the solutions were first diluted 1000 times with 2% HNO_3 (by serial dilution), spiked with indium internal standard, and analyzed in standard solution mode. Sensitivity was around 10 ppb with a relative standard deviation (%RSD) of 2%. Results were measured in ppm and then converted to mol L^{-1}.

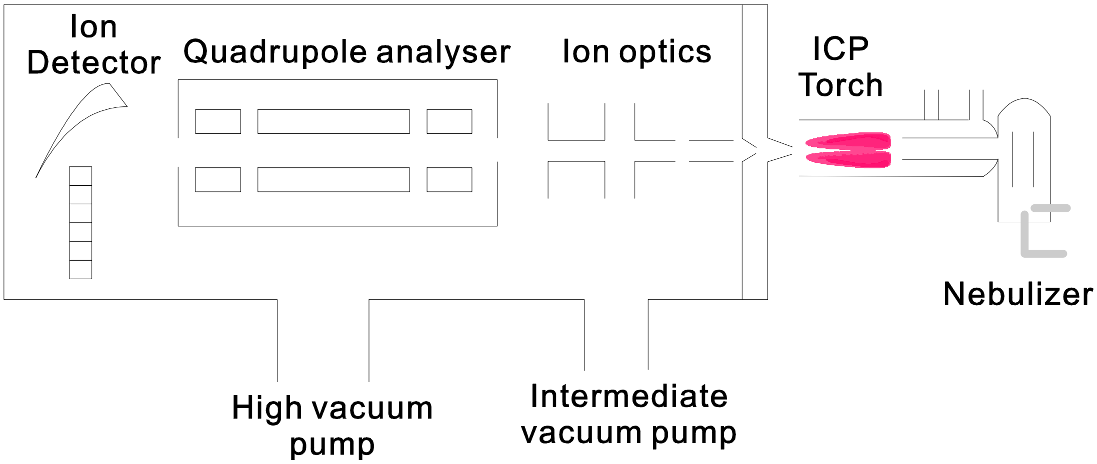

Figure 2.5: Schematic of ICP-MS.

2.4 Atomic force microscopy technique

The atomic force microscopy (AFM) technique provides detailed surface microstructure with atomic resolution. The AFM tip traces the geometric features of the substrate during surface scanning, converting the force exerted by the sample surface to a detectable optical signal. The interactive force between the tip and sample is controlled to be either attractive or repulsive, depending on the application. The AFM doesn't give electronic structure as the scanning tunnelling microscope (STM) does. However, AFM is versatile in studying different types of substrates, such as metals, semiconductors and polymers. The resolution of AFM is largely limited by the size of tip, which is typically 10-100 atoms. With such a bulky tip compared with the size with a single atom, the topography monitored is more atomic periodicity than a true atomic resolution image.

In chapter 5, we propose a metal deposition induced mechanism for Pt electrode dissolution, accompanied by reconstruction and roughening of Pt surface. AFM was used to obtain supporting evidence of the morphology change at the Pt surface. The topography of the Pt surface was imaged by a Veeco Atomic Force Microscope in tapping mode (silicon cantilever, pre-scan with 300 nm resolution for a 200 μm×200

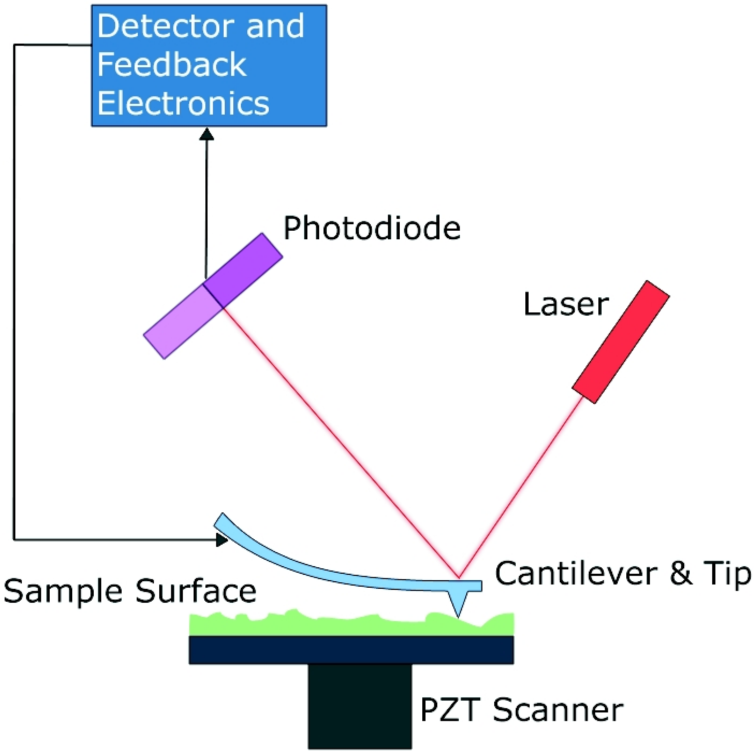

Figure 2.6: Schematic of AFM equipment

μm image area and finalize with 1000 nm resolution for 10 μm×10 μm area). The true-to-geometric roughness factor of the Pt surface was calculated directly from the image by supplementary software, and was typically 1.1-1.8, suggesting a rather smooth surface. These numbers showed good agreement with the roughness factor measured electrochemically by charge measurement in the hydrogen underpotential deposition (UPD) region.

Chapter 3

Effect of variables on EQCM operation

3.1 Introduction

This chapter provides a fundamental look at the behavior of oscillating quartz in contact with liquid, and examines variables which affect the operation of the EQCM and data interpretation in studying electrochemical processes. The applications of QCM to study thin films in vacuum or gaseous phase didn't encounter many difficulties, though a few researchers addressed some operational aspects of using QCM [10, 11]. In most cases, the Sauerbrey model gives an accurate interpretation of the frequency response with few restrictions and modifications. The Sauerbrey equation, showing a linear frequency-mass relationship, has been called into question for its application in liquid media. Nomura et al. [12] observed a substantial frequency drop when introducing the oscillating crystal from the air into the fluid, with its magnitude related to the physical properties of the fluid. Thus it is evident that the frequency response in liquid media can be contributed not only from mass loading on to the crystal surface, but also from liquid loading. Even before this, researchers had been trying to understand the influence of contacting liquid to a resonant QCM. These efforts lead to a few models giving semi-quantitative [13] and quantitative [14–16] descriptions of relations between liquid properties and frequency response, among which the Kanazawa and Gordon model [3] became the most commonly accepted one. Their approach treats the solid-liquid interface as an ideally smooth surface oscillating in contact with a Newtonian fluid. The dampened transverse wave propagates into the liquid from the oscillating crystal surface with a characteristic decay length δ, with

$$\delta = (2\eta_{\mathrm{L}}/\omega\rho_{\mathrm{L}})^{1/2} \tag{3.1}$$

where η_{L} and ρ_{L} are the viscosity and density of the liquid, and ω is the angular oscillation frequency. δ represents the depth of liquid layer probed by the crystal and has a value of 250 nm in 20 °C water with a 5 MHz crystal. It is noteworthy that the electrical double layer, with a typical thickness of ~10 nm, falls well within the detectable boundary layer by a QCM, therefore leading into potential future work exploring the effects of solvent structure and ion adsorption in double layer. Further derivation assuming equal and opposite shear stress on the liquid and quartz sides of the interface gives the famous Kanazawa and Gordon equation:

$$\Delta f = -f_0^{3/2}(\eta_{\mathrm{L}}\rho_{\mathrm{L}}/\pi\rho_{\mathrm{q}}\mu_{\mathrm{q}})^{1/2} \tag{3.2}$$

where f_0 is the resonant frequency of the clean crystal in air. Equation (3.2) gives a quantitative prediction of the frequency shift by liquid contact (about 6 kHz from air into 20 °C water with a 5 MHz crystal), and its remarkable accuracy has made QCM a reliable liquid viscosity/density sensor in many applications. This model, however, describes how liquid contact affects a clean crystal surface, i.e., without mass loading, and thus merely describes the condition prior to mass measurement. The in situ formation of a thin film on the crystal surface causes an additional frequency shift following equation (2.1), giving the total frequency shift in the form:

$$\Delta f = -f_0^{3/2}(\eta_{\mathrm{L}}\rho_{\mathrm{L}}/\pi\rho_{\mathrm{q}}\mu_{\mathrm{q}})^{1/2} - 2f_0^2\Delta m/(\rho_{\mathrm{q}}\mu_{\mathrm{q}})^{1/2} \tag{3.3}$$

or

$$\Delta f = -2f_{\mathrm{s}}^2\Delta m/(\rho_{\mathrm{q}}\mu_{\mathrm{q}})^{1/2} \tag{3.4}$$

where f_{s} is the resonant frequency of a dampened crystal in solution. Equation (3.4), a revised form of equation (2.1), with the effect of liquid contact included in the resonant frequency f_{s}, is valid assuming a small difference between f_0 and f_{s}. In the case of present interest, equation (3.4) is often used as (2.1) itself, provided the in situ calibration constant is carefully determined with electrodeposition or other means.

Difficulties still exist in using the Sauerbrey equation to interpret measured frequency changes in solution. In some cases, the observed frequency change by liquid contact greatly exceeds the Kanazawa and Gordon prediction and can be attributed to non-ideal conditions at the interface, such as surface roughness, interfacial slippage and non-Newtonian liquids. These effects are taken into account by some researchers to develop enhanced liquid loading models [17,18]. In addition, forming a foreign thin film at the solid-liquid interface often causes changes in the double layer structure [2] and therefore the shear wave coupling between the crystal surface and the liquid, thus causing a non-mass-related frequency shift.

In the following sections, I will examine possible variables affecting frequency interpretation and mass measurement. I have made no attempt to give a comprehensive catalogue of them. Many variables contribute minor effects or remain nearly identical throughout an experiment, therefore their effects can be neglected for mass measurement. Some others are identified as variables strongly affecting frequency response and interpretation, and thus need to be discussed in detail. The effects to be discussed in the following section include: effect of temperature, double-layer structure, surface roughness, film non-uniformity and interfacial slippage. Due to the their potential to cause artifacts and errors, some instrumental aspects will also be addressed.

3.2 Temperature effect

The temperature has an effect on the frequency response by influencing both the crystal and solution sides of the interface. The AT-cut quartz for QCM application (cut at an angle of approximately 35°15' from the z-axis of the crystal wafer) has a cubic frequency-temperature characteristic (Eq. 3.5), in contrast to the parabolic characteristic of other crystal cuts (BT, CT, DT, SC, etc.).

$$f/f_0 = a(T - T_0) + b(T - T_0)^2 + c(T - T_0)^3 \tag{3.5}$$

where a, b and c are temperature coefficients at different orders, and T_0 the is inflection temperature, approximately 25 °C. The frequency-temperature curves of AT-cut quartz crystals with slightly different cut angles are given in Fig 3.1. A 20 °C temperature drift from room temperature causes $\approx$ 3 ppm (27 Hz for 9 MHz) shift in resonant frequency, or 1.3 Hz per °C increment. This clearly shows that an AT-cut crystal has a small frequency variation over a wide range of temperatures.

In the other hand, Eq. (3.2) reveals the strong dependence of frequency shift on liquid viscosity and density, and the liquid viscosity and density largely depends on the temperature. The same temperature variation as above for water gives a frequency shift of 393 Hz at 9 MHz, which equals 20 Hz per °C. Comparing with the maximum frequency shift of 25 Hz for cyclic voltammetry in 0.5 M H_2SO_4, it is crucial to have good control of temperature in an EQCM experiment.

Although the temperature of bulk solution and quartz crystal may be well controlled by a thermostat or other technique, dynamic temperature variation may easily occur at microbalance-solution interface. Valentine examined the general case of thermal exchange of the crystal (as heat source by internal friction) with its surrounding

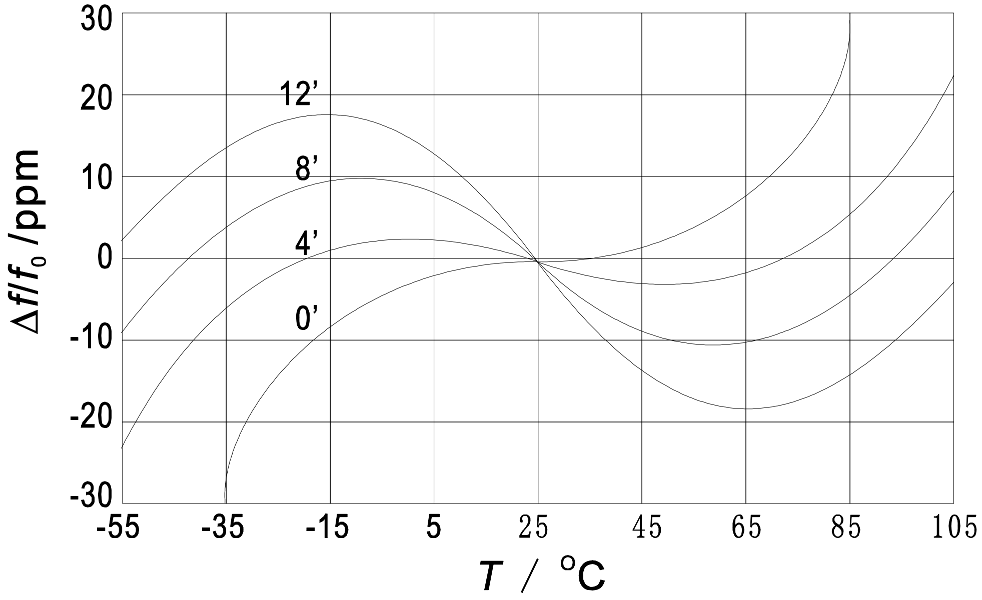

Figure 3.1: Frequency-temperature curve of AT-cut quartz crystal. Figures on top of the curves refer to the deviation of cut angles from 35°15'.

medium, and the resulting frequency shift [19]. In another case, when an electrochemical process takes place at the interface, reversing the direction of an endothermic or exothermic reaction repeatedly by the potentiodynamic method may provide an additional heat source. This effect needs to be taken into serious consideration, and will be discussed in the case of Ag electrodeposition in Chapter 5.

3.3 Double layer structure

The electrical double layer structure can be altered in many ways, chemically or electrochemically, giving additional frequency responses. A potentiodynamic sweep shifts the electrode potential and changes the non-specific adsorption of ions, accompanied by necessary water displacement. Electrodeposition of a thin film often changes the hydrophilicity or hydrophobicity of the surface, resulting in a different profile of adsorbed species. These structural changes give a detectable mass change and frequency shift of the crystal. Raudonis [20] further concluded that only the species present within the outer Helmholtz plane (OHP) would change the electrode mass. As a matter of fact, many researchers have been using EQCM as an important tool to investigate water/ion adsorption at interface. For instance, Santos [21] attributed the small frequency drop in the H UPD region to adsorption of 1 monolayer (ML) of water molecules. There are other changes in double layer in terms of interfacial viscosity and density difference from bulk values, with the presence of surface excess of adsorbates [22], or a depletion layer [23]. However, given the knowledge of how the interfacial structure impacts frequency response, one can extract important double layer structure information from the measured frequency.

3.4 Surface roughness

One important assumption in the Kanazawa and Gordon model is that the crystal surface has to be ideally smooth so that the solid-liquid coupling is a purely viscous effect. The difficulty in preparing such a surface, however, has made most real QCM crystals available with considerable roughness and various microstructures. It is apparent that a crystal surface with sufficient roughness tends to trap a small portion of water in its surface depressions as rigid mass, resulting in a larger frequency shift than that predicted by Kanazawa and Gordon model. Hence, using the Kanazawa and Gordon model for different types of surface morphology must be accompanied by consideration of the roughness effect.

Schumacher [24, 25] has shown that the roughness exerts an influence on the resonance frequency shift in a way similar to solid deposits and liquid contact. In his work, a corrugated surface has been proposed in which the trapped liquid mass is directly related to the frequency change. Although the calculated size of the surface features (30-62 Å) doesn't completely agree with the SEM result (250 Å), his result shows the possibility to correlate surface roughness with its induced frequency shift.

Separate work by some researchers [26–28] has tried to extract roughness information from network analysis of the Quartz Crystal Impedance (QCI). Their results have shown that the rigid and viscous coupling can be distinguished, as represented by parameters related to energy storage and power dissipation in the equivalent circuit of a resonant quartz crystal. Daikhin and Urbakh have reported a more complicated model in a series of papers to elaborate the roughness effect [29–32]. The highlight of this model is its capability to treat a variety of scales of roughness, ranging between two limiting cases of "slight" and "strong" roughness, as represented in Fig. 3.2. Although aiming to treat a nonuniform surface with arbitrary roughness, the authors have demonstrated the necessity to treat the shear wave coupling at interface for the two limiting roughnesses quite differently: a Rayleigh-Fano perturbation theory for slight roughness and Brinkman's equation for strong roughness. Based on this model, the shift in resonant frequency (Δf) and frequency width ($\Delta\Gamma$) measured in liquids with different viscosity and density is fit into the surface roughness profile, i.e., root-mean-square height and correlation length of surface features, assuming the surface is of multiscale roughness. The authors have suggested that the EQCM alone is capable of correlating the surface roughness with frequency measurement, but to achieve the same level of detail as STM in measuring surface roughness, comprehensive impedance spectroscopy analysis is required.

The understanding of the effect of roughness is of great importance in studying surface processes on a roughened or smoothed electrode. For the case of present interest, the surface reconstruction of the Pt electrode surface by repeated oxidizing/reducing cycles, or depositing/stripping Ag monolayers always leads to a change in surface roughness. Our previous work [8] has demonstrated that lower mass than the ideal silver mass for depositing multilayer silver was closely related to electrode smoothing. In this thesis, especially in the studies of Pt dissolution induced by Ag deposition, effort has been made to interpret the frequency data taking into consideration the roughness effect, with direct surface roughness detection by AFM measurement.

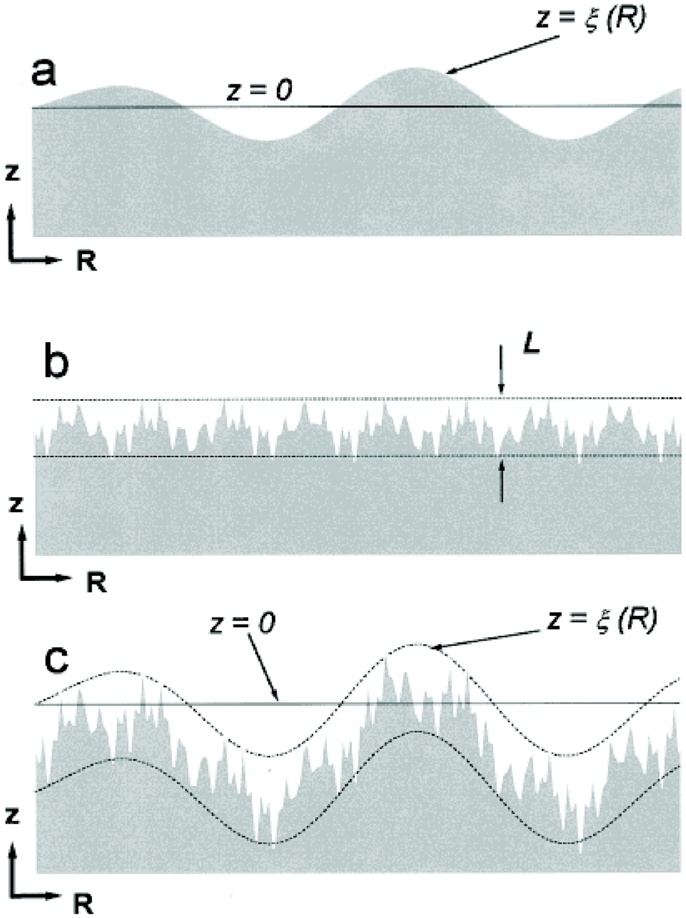

Figure 3.2: Surface with different roughness features: (a) slightly rough surface, characteristic height L (typically 10-100 nm for metallic film on a quartz crystal) much less than lateral feature size; (b) strongly rough surface, L comparable or larger than lateral feature size; (c) surface with multiscale roughness. Reprinted with permission from Ref. [32]. Copyright 2002 American Chemical Society.

3.5 Film non-uniforminty

The Sauerbrey equation assumes uniform mass sensitivity over the entire surface of the crystal, regardless of its location on the surface. It has been demonstrated experimentally, both in gaseous [33] and liquid [34] phases, that the localized mass sensitivity decreases from the center to the edge in a Gaussian distribution manner. Thus the calibration constant C_{f} in Eq. 2.1 is an integral of the differential calibration constant c_{f} over the total surface area of the crystal as:

$$
\begin{aligned}
c_{\mathrm{f}}(r,\theta) &= \mathrm{d}f/\mathrm{d}m && (3.6)\\
C_{\mathrm{f}} &= \int_0^{2\pi}\int_0^{R} c_{\mathrm{f}}(r,\theta)r\mathrm{d}r\mathrm{d}\theta && (3.7)
\end{aligned}
$$

Thus valid application of the Sauerbrey equation requires the deposited thin film to have a uniform thickness, often available from a layer-by-layer growth mechanism. In many cases, electrochemically deposited film grows under a diffusion controlled or surface controlled mechanism. Provided the same surface topology occurs across the active area, the analysis remains valid. As long as the calibration constant C_{f} is calibrated experimentally with some standard procedure, good conformance of frequency data with the Sauerbrey equation can be found. The remaining issue is that for the electrodeposition of a submonolayer film, where the adsorbed molecules are distributed on the electrode surface in a random manner, a variable frequency response is obtained. In such a case, repeating experiments followed by data averaging is a common approach, or estimation of the adsorbate distribution needs to be done. The effect of film non-uniformity will be addressed in Chapter 4, where the initial stage of Pt oxide film formation is investigated.

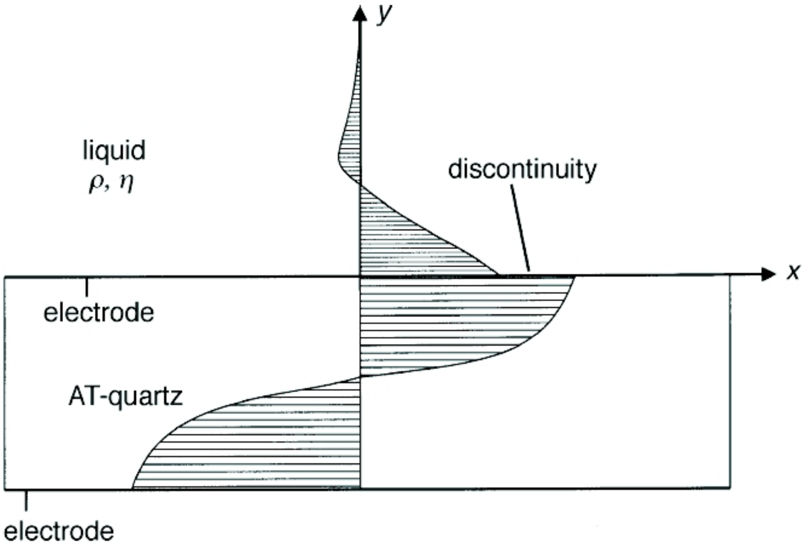

Figure 3.3: The Electrode-liquid interface where interfacial slip occurs. Reprinted with permission from Ref. [35]. Copyright 1997 RSC Publishing.

3.6 Interfacial slip

The Kanazawa and Gordon model describes a "non-slip" condition at the interface, i.e., the first liquid layer is tightly bound to the electrode surface and oscillating at the same velocity as that of the surface. A change in surface energy or interfacial condition, however, may significantly weaken the surface/liquid interaction and lead to a "slip" condition, i.e., a discontinuity of shear velocity from the solid side to liquid side. It is believed that violation of the non-slip condition is possibly caused by a hydrophobic surface oscillating in aqueous solution [36], giving a diminished frequency response compared with a hydrophilic surface. Alternatively, other effects such as small bubble formation [37], or ion/molecular adsorption [38] may be the root cause. The determination of the extent of slip and quantitative correlation with frequency can't be made without consideration of surface roughness due to the pronounced interplay of these factors. Following the earlier model including a complex slip parameter [39] and another four-layer interfacial model [40], recently McHale has reported a complicated model describing the frequency response of a rough surface oscillating under a slip boundary condition [41]. The author argued that if interfacial slip does occur on a rough surface, then it is no longer a molecular level phenomenon, but rather a "hydrodynamic boundary condition". A model was discussed that attempted to mathematically correlate the slip condition with frequency data, but lacks convincing experimental proof. Until now, although many models have been developed to describe the concept of "slip", it still remains experimentally challenging to find direct proof of the slip condition and interpret it.

3.7 Experimental aspects

We now address the experimental aspects of instrument stability and EQCM calibration.

3.7.1 Stability of instrument

The original charm of the EQCM was its extremely high sensitivity (nanogram) in measuring mass accumulation, compared with conventional mechanical or electronic scales. The mass sensitivity of a EQCM is pre-determined by the calibration constant of the quartz crystal and the resolution of frequency counter. For example, a calibration constant of 5.29 ng cm^{-2} Hz^{-1} and a counter resolution of 0.1 Hz in our equipment setup gives a maximum sensitivity of 0.529 ng cm^{-2}. With such a high sensitivity, forming a submonolayer thin film can be easily detected (growing a monolayer of PtO on bare Pt gives 36.3 ng cm^{-2} mass increment). It must be noted that imperfect electromagnetic shielding in the experimental setup can easily cause noise at the 1 Hz level, therefore a certain amount of data smoothing is required to achieve the maximum sensitivity.

In the practical use of EQCM, many researchers have realized the importance of the stability of the instrument in frequency measurement to achieve maximum sensitivity and minimum error in frequency data, especially for detection of submonolayer films. A common instrumental instability is the apparent frequency drift with time, with a magnitude of a few Hz or even larger, when no reaction takes place at the electrode surface or the electrode remains unchanged. It has been confirmed that the temperature drift and aging of the circuit may cause long-term instability, while short-term instability can be ascribed to many affects, such as stress relief between the crystal and the o-rings, temperature fluctuations and random vibrations [42]. The stability of the EQCM in frequency measurement largely depends on instrument design and cell setup, usually independent of the types of electrochemical processes on the electrode. This allows quantitative monitoring of frequency instability in control experiments and subsequent correction of the raw frequency data. It has been observed experimentally that long-term frequency drift that plausibly results from instrument instability may simply reflect constant modification of the electrode surface. In our case, partial dissolution of the Pt electrode under multiple cycles of Ag electrodeposition and stripping leads to a drift that we originally identified as instrumental in origin.

3.7.2 Calibration of the EQCM

To guarantee accurate mass-frequency correlation, i.e., valid interpretation by the Sauerbrey equation, experimental calibration of C_f must be carefully carried out. A few published works have explored some practical procedures for calibrating the EQCM, mostly using metal deposition [43, 44]. Vatankhah et al. reported their results with three conventional electrochemical methods: CV, chronopotentiometry and chronopotentiometry, showing good consistency with these different methods. They emphasized the necessity of experimental calibration of C_f, rather than theoretical calculation from the Sauerbrey equation, prior to performing any frequency measurement. Their findings showed that the actual C_f (4.19 ng Hz^{-1} cm^{-2}) is 25% lower than the calculated one (5.58 ng Hz^{-1} cm^{-2}). Recently, Jeffery et al. [8] used Ag deposition on iodine-covered Pt electrode to determine C_{f}. They argued that a reliable determination of C_{f} and good agreement with the calculated one was achieved due to the role played by uniformly deposited silver at the film-solution interface, because of the unchanging interaction between the iodine and the solutions (silver goes underneath the iodine), and constant electrode surface roughness.

3.8 Conclusions

Deviation from the linear Sauerbrey relation or a slope different from the ideal one may be attributed to one or more effects as discussed above. Care is needed when interpreting frequency response with considerations of these effects. Some effects may not be real, but may nonetheless explain the frequency data quite reasonably. For example, the frequency shift in the H UPD region can be equally well explained by the effect of slip caused by the hydrophilic-to-hydrophobic transition, or by water displacement. Careful interpretation therefore requires knowledge of reaction mechanisms and interfacial properties determined with the help of other in situ techniques.

Chapter 4

EQCM and site blocking studies of Pt oxide growth

4.1 Introduction

The thin oxide film on Pt has been studied using electrochemical methods for about five decades [4–6, 45]. These methods have led to an understanding of the growth kinetics, but the determination of the detailed structure of the film requires surface analytical tools. Many new methods were applied in the last two decades, but the detailed structure remains elusive, particularly for the very first stage of oxidation. One of the difficulties is that the film is not well ordered and so methods such as ex-situ low energy electron diffraction (LEED) and surface X-ray scattering have limited utility. Another difficulty is that there may be a continuum of types of species as the potential is increased [46, 47], and so any particular species is present in very small amounts. Our principal interest here is the initially-formed species that appears to be the oxygen donor in the electrocatalytic oxidation of small organic molecules. This species was suggested very early to be adsorbed OH [48], and this has been the accepted explanation since Conway identified the reversible component seen in dc and ac voltammetry and reflectance measurements [49–51] with adsorbed OH. This reversible component was distinguished from the slower "place exchange" process in which the Pt atom comes out of its metal lattice site.

Direct evidence for the presence of a Pt-OH or other species in the initial stages has been sought by various forms of vibrational spectroscopy [47, 52–57], as discussed below. Although the identity of the oxide species has been controversial, it is significant that there is no spectroscopic evidence for a distinct species at the very beginning of the oxidation (ca. 0.8 V) that is different from the species at higher potentials where the "place-exchange" occurs. This may just be an indication that spectroscopic methods are insufficiently sensitive, and it is noteworthy that the reflectance and kinetic evidence only suggested that a fraction of the early oxidation, ca. 0.3 ML [58], was attributed to the reversible OH component. However, it may be instead that there is no distinct species associated with the initial stage. In support of this, Harrington repeated the ac voltammetry experiments [46], but at many frequencies and argued that there was no kinetic evidence for a faster component. Likewise, a single simple rate law can explain results from many types of experiments [59]. A single process in which the Pt atoms leave their metal lattice sites to become Pt(II) species was suggested as the sole process in oxide growth up to ca. 1.5 V. Simulations of such a process showed the correct growth rate law but the parameters were not in quantitative agreement with experiment [60]. In this model, the reversible component is attributed not to a faster process but to the ability of Pt atoms to return to their original lattice sites only in the earliest stages of film growth.

We here address this issue using the electrochemical quartz-crystal microbalance (EQCM), coupled with probe molecules (e.g., H_2) in the solution that count uncovered Pt sites. Nernst [61] and Sackur [62] first found that the rate of the hydrogen oxidation reaction (HOR) significantly decreases in the potential region where oxide film is formed on the Pt surface. Early work by Breiter [63] examined the reaction rate of the HOR as a function of potential in 1 M H_2SO_4, under both potentiodynamic and potentiostatic conditions. The correlation between the decreasing total current in H_2 saturated solution and oxygen coverage (calculated by cathodic charging) in the potential region between 0.8 and 1.1 V lead to his conclusion that the inhibition of HOR was due to forming a small oxygen coverage (less than 0.5). Starting from these observations, we refined a method using H_2 as a candidate molecule for direct probing of the oxygen coverage change during the initial stage of Pt oxidation, by analyzing the CV currents with and without H_2 present. The EQCM has sufficient sensitivity to address the nature of the oxidation species, and was used by Birss [64] to show that the species formed was either PtO or PtO_2, but could not be a hydroxide film. This study measured only the reduction of thicker films, but did not address the initial film formation stage. EQCM work by Conway, Jerkiewicz, and their coworkers [65, 66] led to the suggestion that the initial oxidation species is a bridging adsorbed oxygen, and Conway concluded that adsorbed OH was not part of a two-step oxidation mechanism [67]. Here we provide evidence supporting for the existence of an adsorbed oxygen atom, though our analysis of the EQCM data proceeds via a different methodology.

4.2 Site-blocking experiment with H_2 as probe molecule

The Pt cyclic voltammogram (CV) in the 0.5 M H_2SO_4 solution with a fine H_2 stream of bubbles is shown in Fig 4.1. It is assumed that the solution is saturated with H_2 and has a constant H_2 concentration. The CV of the H_2-free H_2SO_4 solution with Ar bubbling is shown as a baseline. The CV baseline has three distinctive potential regions of a clean Pt surface: 0.05-0.3 V for underpotential deposition/desorption of hydrogen, 0.35-0.8 V for double layer charging and 0.85-1.5 V for oxidation/reduction of the Pt oxide. The CV with the presence of H_2 in solution shows similar features as a clean Pt electrode, but the current is apparently elevated (approximately 30

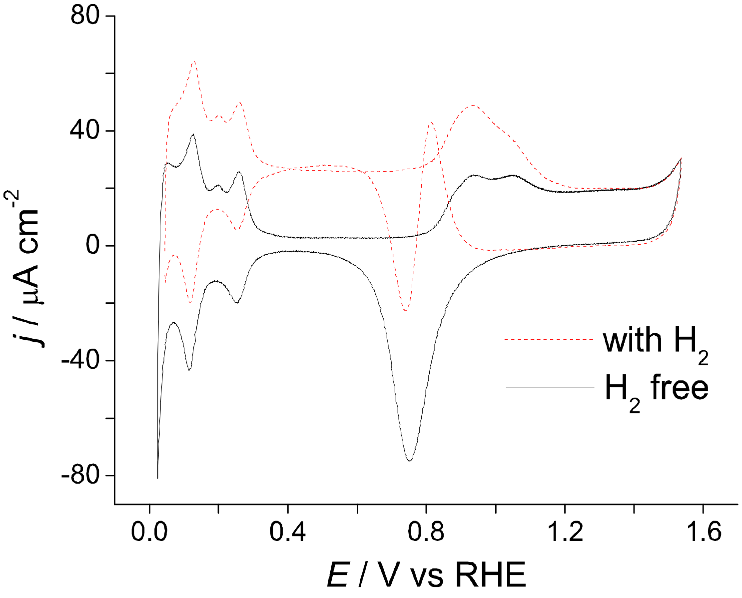

Figure 4.1: Comparison of Pt cyclic voltammograms in hydrogen-free solution (black and solid trace) and in hydrogen-saturated solution (red and dashed trace). 0.5 M H_2SO_4, 20 mV s^{-1}.

μA cm^{-2} higher than baseline) over the potential region up to 1.2 V. This elevated current, $j_{\mathrm{H_2}}$ includes the baseline current reflective of the properties of Pt surface, and an additional current component, j_{ox} from the oxidation of dissolved H_2 at the Pt electrode. The H_2 oxidation reaction (HOR) takes place at any potential higher than 0 V via the following elementary steps [68]:

$$\mathrm{H_2(aq) + 2Pt} \leftrightarrows \mathrm{2\ PtH(ads)}, \text{ Tafel reaction} \tag{4.1}$$

$$\mathrm{H_2(aq) + Pt} \leftrightarrows \mathrm{PtH(ads) + H^+ + e^-}, \text{ Heyrovsky reaction} \tag{4.2}$$

$$\mathrm{PtH(ads)} \leftrightarrows \mathrm{Pt + H^+ + e^-}, \text{ Volmer reaction} \tag{4.3}$$

Here Pt indicates a free site for adsorption, with the implicit assumption that the fully-covered surface has one H per Pt atom. The oxidation of H_2 is initiated by the adsorption of H_2 on a free Pt site, i.e., uncovered by oxide film, in a dissociative (Tafel) or oxidative (Heyrovsky) way, followed by one-electron oxidation (Volmer) of the adsorbed H species. For either pathway, the reaction involves an adsorbed intermediate and thus continuous oxidation depends on the availability of free Pt sites. The rate of the HOR is sufficiently fast to bring the current to the mass-transport limited value at a small overpotential, as manifested in the horizontal component to the current even at ca. 50 mV in Fig 4.1. In the potential region above about 0.75 V, the Pt surface becomes gradually oxidized and covered by a thin oxide film, which blocks the free Pt sites and prevents H adsorption and H_2 oxidation. The progressive oxidation leads eventually to the complete cessation of the HOR and the currents with and without H_2 are then the same.

We see here that the mass-transport-limited H_2 oxidation current density, j_{ox}, is intrinsically controlled by the number of free Pt sites rather than by the potential. Therefore it may be utilized as a tool to probe the number of free Pt sites, particularly in the initial stage of oxide film formation where the number of free Pt sites starts to decrease. The j_{ox} reported here is measured relative to the true electrode area,

A_t (0.235 cm^2 for the Pt electrode on the quartz crystal). The maximum limiting oxidation current density, $j_\mathrm{ox,\ max}$ is given by the usual expression:

$$j_\mathrm{ox,\ max} = \frac{2FDC^*}{\delta} \tag{4.4}$$

and

$$j_\mathrm{ox} = (1-\theta) j_\mathrm{ox,\ max} = \frac{2(1-\theta)FDC^*}{\delta} \tag{4.5}$$

where δ is the thickness of diffusion layer and θ is the fraction of the surface covered by oxide. In the presence of site blocking, the current is attenuated by the factor $(1-\theta)$, that is the fraction of the surface covered by free sites. In the solution saturated with H_2 at a well stabilized temperature, the parameters D, C^* and δ are considered as constants. Therefore $1-\theta$ as a function of potential may be extracted experimentally as the ratio $j_\mathrm{ox}/j_\mathrm{ox,\ max}$. It is evident that the coverage $1-\theta$ obtained this way is a fractional surface coverage, i.e., the fraction of area or number of sites on the clean surface. The difficulty arises in the determination of j_ox in a potentiodynamic process, where the measured current must first be corrected for other faradaic or charging currents.

We make the simple assumption that the other processes are identical in the presence and absence of H_2, so the j_{H_2} is simply a sum of two current components, i.e., the j_ox can be calculated by subtraction of the baseline current from j_{H_2}. The calculated j_ox in the positive-going sweep at different sweep rates is given in Fig 4.2. At a low sweep rate of 2 mV s^{-1}, the j_ox measured in a linear potential sweep can be effectively regarded as the steady state current-potential relationship. A limiting j_ox of $\sim$25 μA cm^{-2} was observed over a wide range of potentials from 0.05 V to 0.85 V. This clearly shows that the HOR is controlled by mass transport and the free Pt area remains unchanged at 1 ($\theta = 0$). When the potential is increased above 0.85 V, j_ox drops quickly until it reaches a small residual current of $\sim$2.3 μA cm^{-2}. This indicates that the oxidation of Pt surface occurs with an onset potential of 0.85 V,

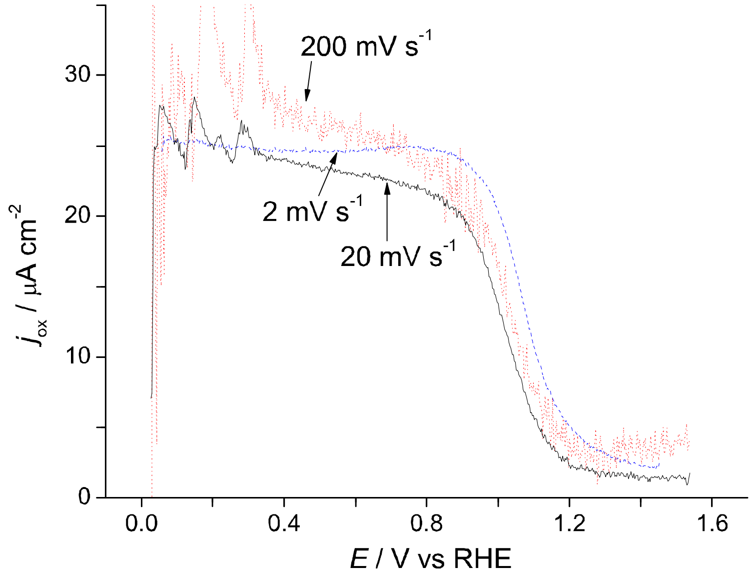

Figure 4.2: The H_2 oxidation current, j_{ox} measured in a positive-going sweep at different sweep rates. Pt electrode, 0.5 M H_2SO_4.

and is followed by quick population of the free Pt sites by species in the oxide growth process. The small residual oxidation current at higher potential (E >1.4 V), rather than $j_{\text{ox}} = 0\ \mu\text{A cm}^{-2}$ as expected suggests that a small quantity of HOR may still take place. It is not clear whether this occurs on remaining free sites, if the HOR can occur on the fully covered surface, or if the residual current is due to slightly different surface composition in the presence and absence of H_2.

The j_{ox} feature measured at faster sweep rates of 20 mV s^{-1} and 200 mV s^{-1} apparently includes some dynamic effects. A slightly decaying limiting current was observed at these sweep rates, and the higher sweep rate results in a faster decay. However, the average limiting j_{ox} at sweep rates from 2 mV s^{-1} to 200 mV $^{-1}$ is roughly the same and j_{ox} begins to drop at the same onset potential of 0.85 V. At higher sweep rates, the j_{ox} reaches a constant residual current at 1.2 V where the residual current becomes less than 10% of the diffusion controlled j_{ox} at 0.85 V, compared with at 1.35 V at 2 mV s^{-1}. This may be caused by the convective mass transport by the bubbling, which has a more significant influence in a quasi-steady-state experiment (sweep rate of 2 mV s^{-1}) than in a potentiodynamic experiment (higher sweep rate). If we assume the constant residual current indicates a Pt surface fully covered by oxide film, this potential E_{m} represents the point in the initial stage of oxide growth where a full monolayer is formed, and needs to be carefully determined free of artifacts by some special technique.

4.3 RDE studies of initial oxide film formation

The above experiments were carried out with a fine H_2 stream of bubbles without apparent disturbance of the solution. Experiments showed that the limiting j_{ox} increased continuously with increasing bubbling rate until it became noisy, and this suggested that either the solution was not completely saturated by the fine H_2 stream, or there was a convective component to the limiting j_{ox}. Rotating disk electrode (RDE) experiments were performed to study the convective component to the limiting current and determine the actual H_2 concentration. CVs for saturated H_2 solutions at different rotation rates are shown in Fig 4.3. The positive-going j_{H_2} has a plateau-to-plateau feature, showing a clear transition from mass transport limited HOR to the cessation of HOR (although as before there is a small residual current). Such large currents can be understood as the result of the significantly decreased diffusion layer thickness δ in Eq. (4.4) caused by the rotation of the electrode surface. In this context, two approaches are available for the calculation of j_{ox}: one is by removal of the baseline current at the same rotation rate and the other is by extrapolation using j_{H_2} at different rotation rates.

The first approach follows the same idea as discussed in the previous section, but improves the j_{ox} feature because the convective component by the bubbling is now negligible. Fig 4.4 gives the j_{ox} features at a few representative rotation rates.

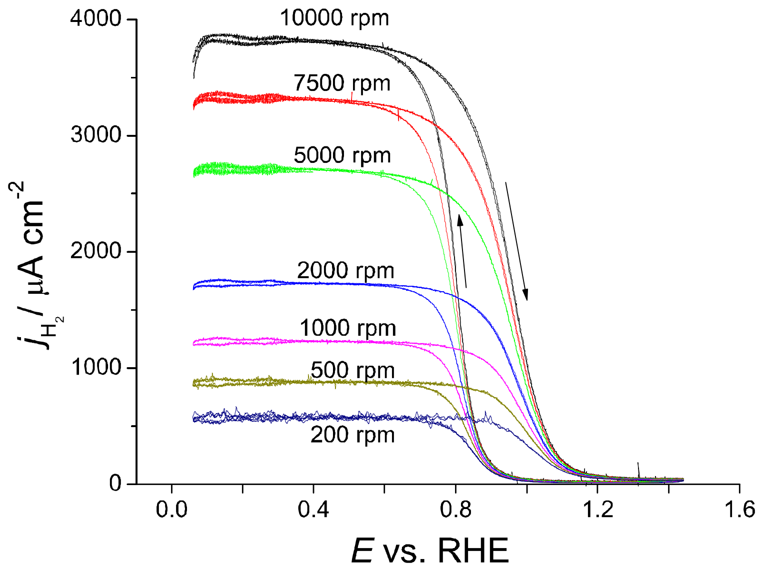

Figure 4.3: Pt CVs with a fine H_2 stream in 0.5 M H_2SO_4 solution, sweep rate 20 mV s^{-1}, rotation rates from 200 to 10000 rpm.

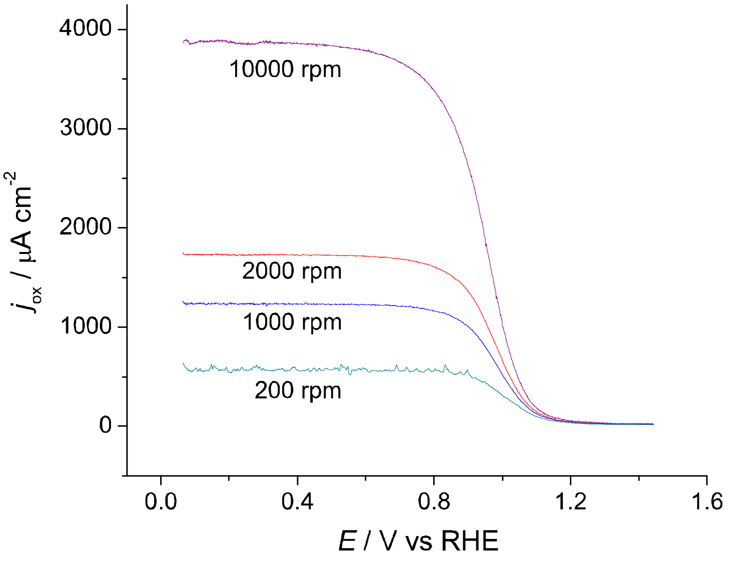

Figure 4.4: j_{ox} in 0.5 M H_2SO_4 saturated with H_2, sweep rate 20 mV s^{-1} (positive-going), rotation rate at 200, 1000, 2000 and 10000 rpm, respectively.

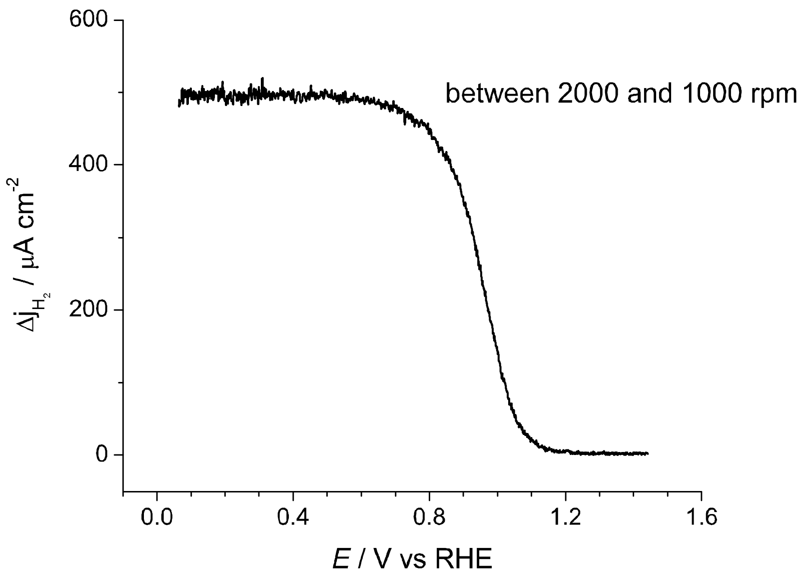

Figure 4.5: Differential current between rotation rate of 2000 and 1000 rpm in 0.5 M H_2SO_4 saturated with H_2, sweep rate 20 mV s^{-1}, positive-going sweep.

The j_{ox} behaviour in the initial stage of oxide thin film formation is apparently affected by the rotation rate: the current begins to decrease earlier at higher rotation rate, e.g., 0.60 V at 10000 rpm compared with 0.85 V at 200 rpm (at rotation rates lower than 200 rpm, the j_{ox} is significantly distorted by a noise component, but faithfully indicates an onset potential of 0.85 V for Pt oxide formation). By contrast, j_{ox} reaches a constant residual current at a monolayer completion potential E_{m} between 1.15 V and 1.2 V, showing little dependence on rotation rate.

The second approach is based on the assumption that the RDE current difference ($\Delta j_{\mathrm{H_2}}$, used instead of j_{ox} in this approach) between two different rotation rates only includes the mass-transport-controlled current component from HOR, and any kinetic-controlled current component (such as ion adsorption and oxidation of Pt) will be removed since it is independent of rotation rate. Fig 4.5 gives an example of $\Delta j_{\mathrm{H_2}}$ between rotation rates of 2000 rpm and 1000 rpm. The $\Delta j_{\mathrm{H_2}}$curve indicates an onset potential for Pt oxide formation at 0.65 V, close to the onset potential by j_{ox} at 2000 rpm. The effect of rotation rate on the onset potential doesn't cancel out by differencing the $j_{\mathrm{H_2}}$ at different rotation rates. This suggests that correct determination of the onset potential of oxide film formation probed by H_2 needs to be done in a stagnant solution, or at low rotation rate in an RDE experiment. This second approach using a $\Delta j_{\mathrm{H_2}}$ curve has great advantage over the first approach by showing a definite E_{m} at 1.15 V with a residual current of nearly zero. To determine the oxidation state and the possible composition of initially-formed Pt oxide thin film, EQCM experiments will be performed, accompanied by frequency and charge analysis in Section 4.6.

4.4 O_2 as probe molecule

The above experiments explored the possibility of probing the surface coverage change of initial Pt oxide formation in a simple way. The H_2 molecule is a suitable probe molecule to investigate oxide film formation, because of facile HOR on Pt with little interference to the growth of the oxide film. Other candidate molecules that have similar electrochemical properties to H_2, ranging from simple gas molecules to organic molecules, could be used in our methodology. Here we evaluate the capability of O_2 as a probe molecule. The CV in 0.5 M H_2SO_4 solution with O_2 bubbling is shown in Fig 4.6, with H_2SO_4 solution deoxygenated by bubbling argon as baseline. The large current shift in the low potential region ($E < 0.9$ V) is due to the O_2 reduction reaction (ORR) on the Pt surface:

$$\mathrm{O_2 + 4H^+ + 4e^- \rightarrow H_2O},\ E_1^{\mathrm{o}} = 1.23\ \mathrm{V} \tag{4.6}$$

$$\mathrm{O_2 + 2H^+ + 2e^- \rightarrow H_2O_2},\ E_2^{\mathrm{o}} = 0.695\ \mathrm{V} \tag{4.7}$$

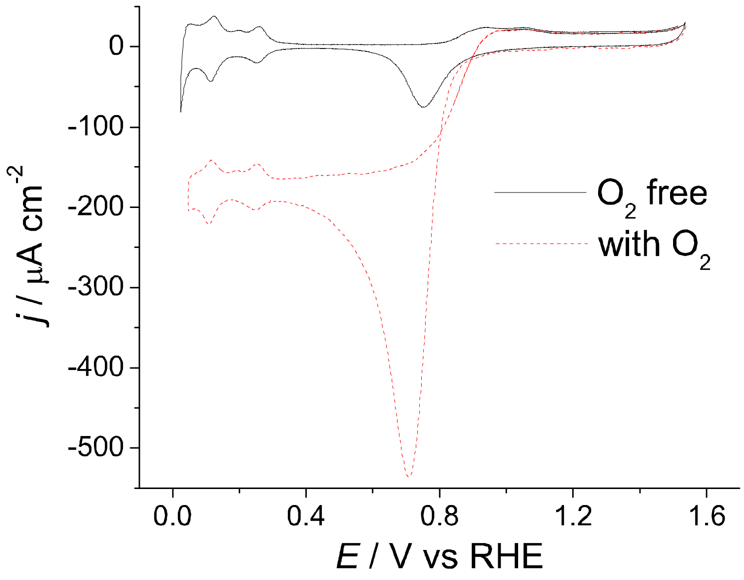

Figure 4.6: Comparison of Pt cyclic voltammograms in oxygen-free solution (black and solid trace) and in oxygen-saturated solution (red and dashed trace). 0.5 M H_2SO_4, 20 mV s^{-1}.

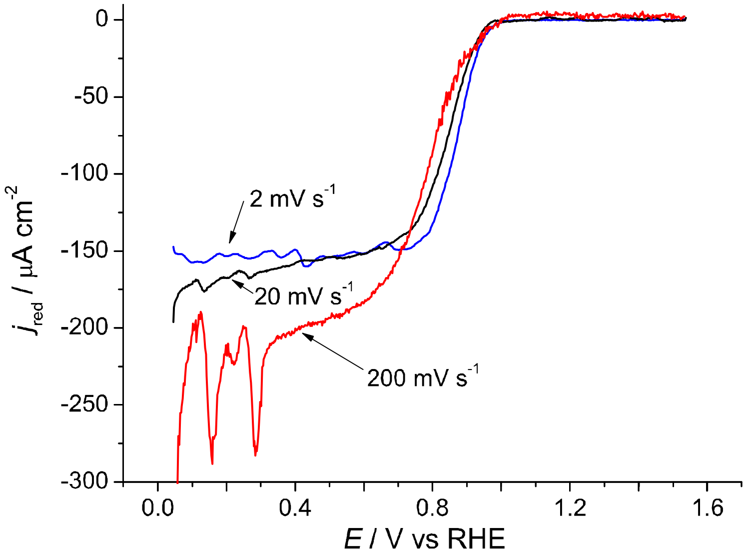

Figure 4.7: The O_2 reduction current, j_{red}, measured in a positive-going sweep at different sweep rates. Pt electrode, 0.5 M H_2SO_4.

i.e., complete four-electron reduction to water or two-electron reduction to peroxide. Both reactions occur in O_2 containing solutions at potentials lower than E_2°, and often one dominates the overall reaction. The mechanism for ORR catalyzed by Pt surface includes many possible elementary steps with a variety of adsorbed intermediates: Pt-OOH, PtOHOH, PtOH, PtO, etc. [69]. The second reaction has been frequently observed when the Pt surface is occupied by adsorbed atoms such as bisulfate. The dominant reaction in our system will be determined later by RDE experiments. The reduction current of O_2 (j_{red}, similar to the j_{ox} of HOR) is calculated by subtracting the baseline current in deoxygenated solution from the CV current in O_2 containing solution (j_{O_2}), as shown in Fig. 4.7. At a sweep rate of 2 mV s^{-1}, a relatively larger mass-transport-limited j_{red} of -160 μA cm^{-2} at $E < 0.75$ V was obtained compared to the H_2 case. This is due to the different physical properties of O_2 in solution from H_2 (solubility, diffusion coefficient, diffusion layer length, etc.) and the greater number of electrons in the reaction. The noise component in this limiting current suggests that the stagnant solution is not free of convective mass transport. The noise component is improved at sweep rates higher than 20 mV s^{-1}. The reduction current j_{red} begins to decay (upward shift in Fig. 4.7) at $E > 0.75$ V, caused by either the growth of the Pt oxide film, or by switching off the ORR current as the potential is raised higher than the reversible potential near $E_2^{\mathrm{o}} = 0.695$ V. At a sweep rate of 200 mV s^{-1}, j_{red} begins to decay at a lower potential of 0.65 V. On the other hand, j_{red} reaches a residual current of < 1 μA cm^{-2} at 1.0 V, regardless of the sweep rate. At potentials higher than 1.0 V, the ORR completely ceases and the only active electrochemical process is further formation of Pt oxide. Compared with the initial stage of oxide formation at 0.85 V to 1.15 V as probed by H_2, it is clear that the growth of Pt oxide film in the initial stage occurs at more negative potentials with O_2 in solution. The free Pt sites profile (1–θ) which can be calculated from the j_{red} feature, seems to be a special case with the presence of O_2 in solution, and does not reflect the situation in the deoxygenated solution.

Although O_2 appears to be a less useful probe molecule than H_2, we performed the same series of RDE experiments to determine the reliability of j_{red}. Fig. 4.8 shows j_{red} at a few representative rotation rates. Similar to the RDE results for H_2-containing solution, j_{red} measured at higher rotation rates in O_2-containing solution shows a lower apparent onset potential of Pt oxidation. Furthermore, at rotation rates as high as 9999 rpm, j_{red} is no longer controlled by mass transport, showing a flat trace in the low potential region, but gradually decaying for $E > 0.3$ V. At most rotation rates, j_{red} decays to a residual current at 0.95 V, where ORR ceases. Again the differential RDE current ($\Delta j_{\mathrm{O_2}}$) at rotation rates of 2000 and 1000 rpm helps to clarify the mass-transport-controlled current component. As shown is Fig. 4.9, $\Delta j_{\mathrm{O_2}}$ reaches a residual current at 0.85 V, where the ORR (possibly in the four-electron pathway) becomes no longer controlled by mass transport. Between 0.85 V and 0.95 V, the kinetically controlled ORR current gradually decreases until its complete cessation at 0.95 V where the free Pt sites have been fully occupied by oxide

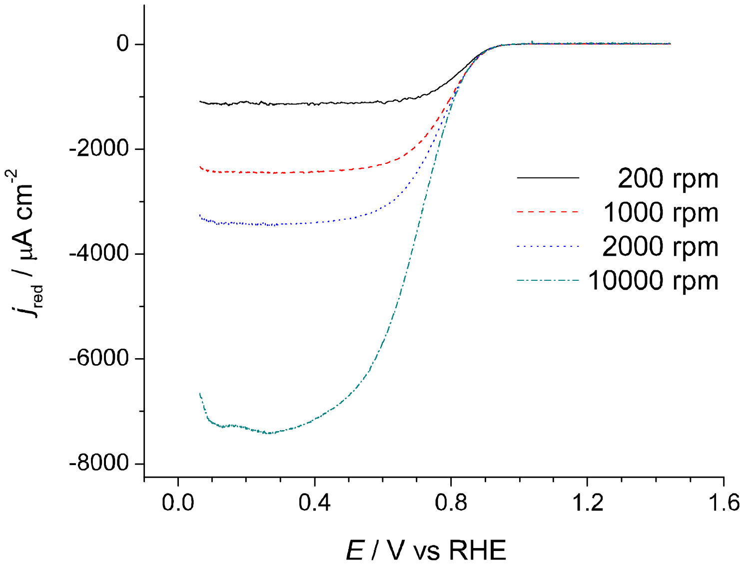

Figure 4.8: j_{red} in 0.5 M H_2SO_4 saturated with O_2, sweep rate 20 mV s^{-1} (positive-going), rotation rates 200, 1000, 2000 and 10000 rpm.

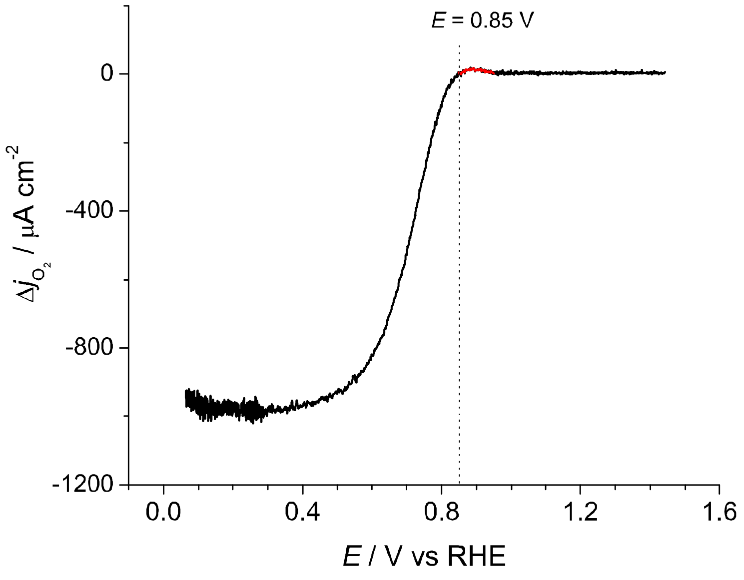

Figure 4.9: RDE current difference between rotation rates of 2000 and 1000 rpm in 0.5 M H_2SO_4 saturated with O_2, sweep rate 20 mV s^{-1}, positive-going sweep.

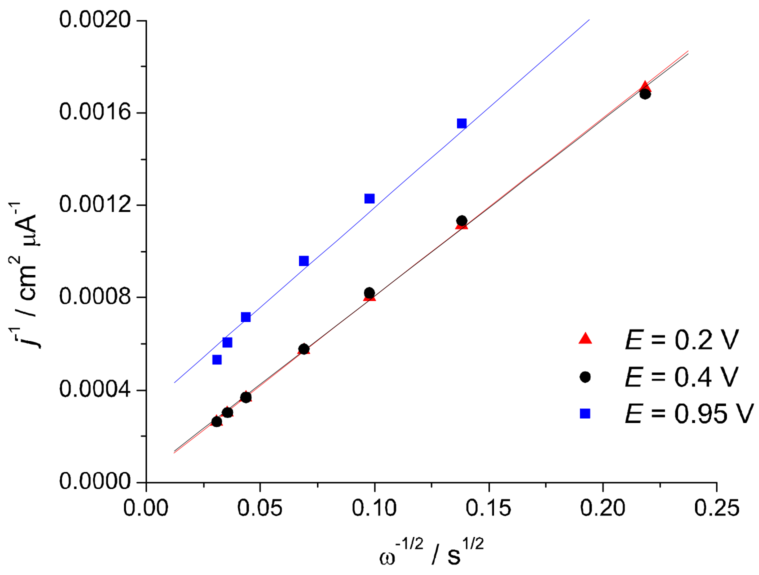

Figure 4.10: Correlation of RDE current and rotation rate at $E = 0.2$, 0.4 and 0.95 V. H_2-saturated 0.5 H_2SO4, 20 mV s^{-1}, positive-going sweep.

film species.

4.5 Determination of actual H_2 and O_2 concentration

The RDE experiment has so far provided valuable information to support the probing of the initial oxide film formation by H_2. As discussed in Section 2.2, the RDE is an important method to determine the property of solutions according to Eq. (2.3), e.g., the bulk concentration of electrochemical active species. The current density j_{H_2} is used to determine the actual H_2 concentration in H_2SO_4, by plotting $j_{H_2}^{-1}$ against $\omega^{-1/2}$ at a diffusion controlled potential, as shown in Fig. 4.10. The slope of the curve, which equals $(0.620nFC_0^*D_0^{2/3}\nu^{-1/6})^{-1}$ according to Eq. 2.3, is determined to be 0.00763 cm^2 μA^{-1} s$^{-1/2}$, with $R^2 = 0.9992$. For H_2 in 0.5 M H_2SO_4, $n = 2$

because there are two electrons transferred per H_2 molecule; $D_0 = 2.79\times10^{-5}$ cm^2 s^{-1}, calculated from the Wilke-Chang equation [70]:

$$D_{\mathrm{H_2\text{-}H_2O}} = 7.4 \times 10^{-8}\frac{T(\psi_{\mathrm{H_2O}} M_{\mathrm{H_2O}})^{1/2}}{\eta V_{\mathrm{H_2}}^{0.6}} \tag{4.8}$$

where $T = 298.13$ K, $\psi_{\mathrm{H_2O}}$ the association parameter for water = 2.26, $M_{\mathrm{H_2O}} = 18$ g mol^{-1}, η the viscosity for water = 1.002 Pa s and $V_{\mathrm{H_2}}$ the molar volume of H_2 = 14.3 cm^3 g^{-1} mol^{-1}; $\nu = 0.0108$ cm^2 s for H_2O or diluted solution; $F = 96485$ C mol^{-1}. The H_2 concentration with a fine H_2 stream was calculated to be $C_0^* = 4.89\times10^{-4}$ M, 36% less than the theoretical saturated concentration of 7.68×10^{-4} M in water (the saturated concentration in 0.5 M H_2SO_4 is estimated to be 6% less than that in pure water). However, the use of j_{ox} as an indication of free surface coverage doesn't require a saturated solution, but merely a stable H_2 concentration. The $j_{\mathrm{H_2}}$ (and later $j_{\mathrm{O_2}}$) in our CV experiments remained identical on successive cycles, suggestive of no H_2 (or O_2) time-dependent concentration change in solution.

The O_2 concentration was determined by plotting the reciprocal of the limiting current at a potential where the RDE current is controlled by mass transport against $\omega^{-1/2}$, as shown in Fig. 4.11. Assuming the four-electron transfer pathway, a slope of 0.00385 cm^2 μA^{-1} s$^{-1/2}$ ($R^2 = 0.9995$) gives the actual O_2 concentration of 1.18×10^{-3} M, in good agreement with the tabulated concentration of 1.23×10^{-3} M in 0.5 M H_2SO_4 [71].

4.6 Charge and Frequency analysis

The total charge for Pt oxidation in the early stage, determined from current integration, can be directly used for the calculation of the oxidation state, or the average oxidation state if multiple species exist. The total current needs to be corrected for double layer charging to leave the faradaic component. We assume insignificant

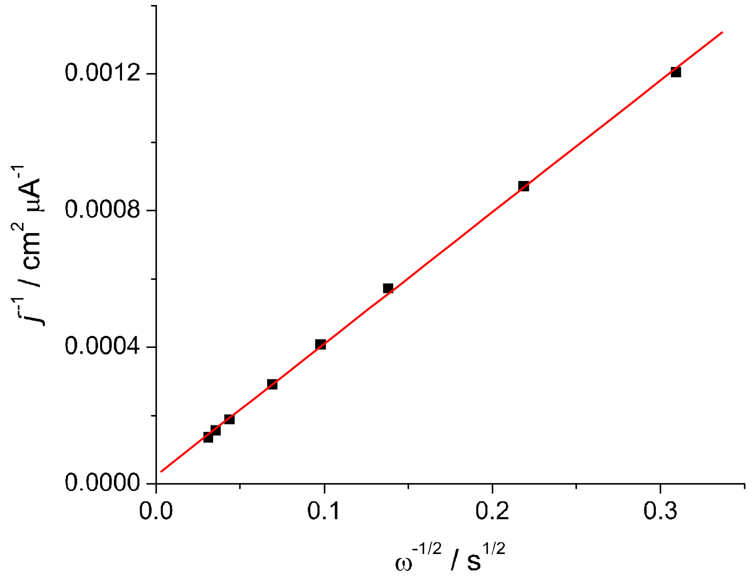

Figure 4.11: Correlation of RDE current and rotation rate at E = 0.25 V. O_2-saturated 0.5 H_2SO_4, 20 mV s^{-1}, positive-going sweep.

change in double layer structure from the double layer region through the initial stage of oxidation, i.e. the double layer charging current, j_{dl}, in the initial stage is taken as the same flat baseline as in double layer region (see Fig 4.12). The charge density for one-electron oxidation of Pt electrode is assumed to be 220 μC cm^{-2} per Pt. The oxidation state for Pt in the early stage (0.85 V to 1.15 V), i.e., the number of electrons per Pt atom, was determined to be 1.27±0.06, which supports one-electron oxidation for the overall early stage. The slight deviation may be oxidation of trace organic impurities but is also likely to be caused by starting to grow a second monolayer of oxide film before the first monolayer is complete. Assuming that neither of these complications occur, the value of 1.27 implies 27% of two-electron oxidation and 73% of one-electron oxidation.

The EQCM frequency data showing simultaneous current and mass change helps to identify the mechanism of surface processes and the nature of surface species. The

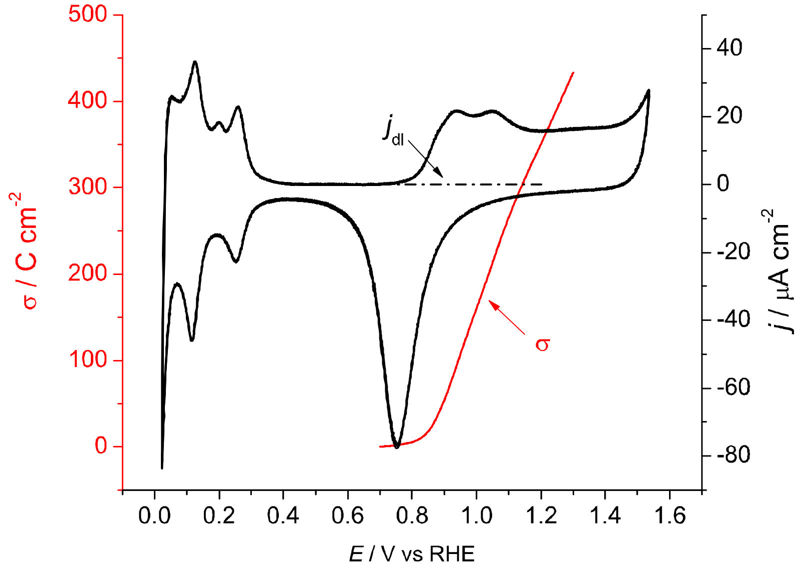

Figure 4.12: Pt cyclic voltammograms in 0.5 M H_2SO_4 solution (black trace) and the calculated charge density for Pt oxidation (corrected for double layer charging) as a function of potential (red trace). Sweep rate 20 mV s^{-1}.

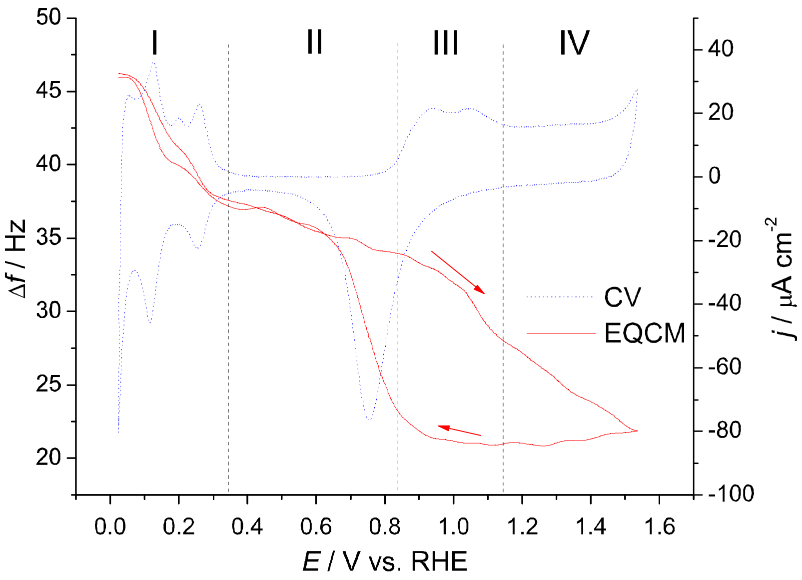

Figure 4.13: Pt cyclic voltammogram in 0.5 M H_2SO_4 solution (black trace) and simultaneously recorded frequency shift (Δf) as a function of potential (red trace). sweep rate at 20 mV s^{-1}.

frequency response recorded over a single potential cycle is shown in Fig. 4.13. For the positive-going sweep, the overall potential region can be divided into four different stages according to the current features: the hydrogen UPD region (stage I, 0.05 V to 0.35 V), the double layer region (stage II, 0.35 V to 0.85 V), the early stage for Pt oxide formation (stage III, 0.85 V to 1.15 V) and the further oxidation region (stage IV, 1.15 V and higher). The frequency shifts in each stage result from the mass change at the interface due to different surface processes. The mass change (calculated from Eq. (2.1)) and responsible surface species for each stage are listed in Table 4.1.

The overall mass change in each stage could be due to multiple processes taking place on the electrode surface, e.g., the 18±2 ng cm^{-2} mass accumulation in the double layer region appears to result from the adsorption of water and bisulfate, but the ratio between these two species can't be clearly identified. However, the surface

Table 4.1: Mass change and responsible surface species in each stage during the positive-going sweep

Stage	Definition	Δm / ng cm^{-2}	Responsible surface species
I	H UPD	46±5	H, H_2O
II	Double layer	18±2	H_2O, HSO_4^-
III	Initial stage	28±3	OH or O^{2-}
IV	Further Oxidation	37±4	O^{2-}

species can be distinguished by its molar mass per electron, M_e, e.g., 17 g mol^{-1} for OH^- and 8 g mol^{-1} for O^{2-}, and therefore a convenient method to quantitatively identify the surface species is by correlating the mass (or frequency by EQCM) with charge density related to forming or replacing such a species:

$$\Delta m = \frac{\Delta\sigma}{nF} M \tag{4.9}$$

or:

$$M_\mathrm{e} = \frac{M}{n} = \frac{F\Delta m}{\Delta\sigma} = C_\mathrm{f} F \frac{\Delta f}{\Delta\sigma} \tag{4.10}$$

where Δm is the mass change per unit area, $\Delta\sigma$ is the charge density, n is the number of electrons and M is the molar mass. The charge density was used without correction for the double layer effect. The reason is simply that the double layer charging current is reflective of the ion adsorption, and anion-adsorption-induced frequency component is likely included in the total frequency response. Removing the double layer charging current from the total current leads merely to a larger M_e. The frequency shift vs. charge density plot for the data of Fig. 4.13 and the determined M_e for each stage is presented in Fig. 4.14. An M_e of 9.1±0.9 g mol^{-1} in stage I is assigned to H_2O adsorption, since adsorbing or desorbing H doesn't result in this high a molar mass change. The free Pt sites released from the oxidative desorption of hydrogen adatoms are immediately occupied by water molecules:

$$\mathrm{PtH} + x\mathrm{H_2O} \rightarrow \mathrm{Pt(H_2O)}_x + \mathrm{H^+} + \mathrm{e^-} \tag{4.11}$$

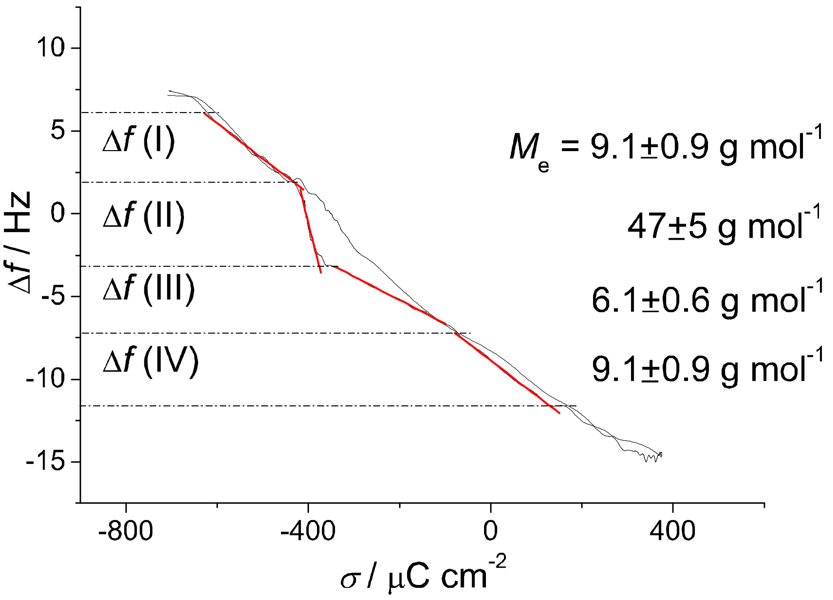

Figure 4.14: Frequency shift vs. charge density. Distinctive slop at each stage indicates surface species of distinctive molar mass per electron (M_e).

The overall process gives an M_e of (18x-1) g mol^{-1}. The fractional coverage of water molecules per Pt. The M_e of 9.1±0.9 g mol^{-1} in stage I clearly indicates $x \approx 0.56$ and each Pt site is covered by half a water molecule right before the double layer region.

An M_e of 47±5 g mol^{-1} was observed in the double layer region, due to $\mathrm{HSO_4^-}$ adsorption:

$$\mathrm{Pt(H_2O)_x} + y\mathrm{HSO_4^-} \rightarrow \mathrm{Pt(H_2O)}_{x'}\mathrm{(HSO_4)}_y + (x - x')\mathrm{H_2O} + y\mathrm{e^-} \tag{4.12}$$

The specific adsorption of $\mathrm{HSO_4^-}$ is coupled with $\mathrm{H_2O}$ displacement, since adsorption of $\mathrm{HSO_4^-}$ species gives a much higher M_e of 97 g mol^{-1}. The overall process gives a M_e of $(97y\text{-}18\Delta x)/y$ g mol^{-1}, where $\Delta x = x - x'$ is the fractional water desorption per Pt. The 47±5 g mol^{-1} in stage II indicates that the adsorption of each bisulfate is accompanied by desorption of approximately three water molecules, which gives an M_e of 43 g mol^{-1}. The actual amount of bisulfate adsorption needs to be determined by other methods, e.g. using radiotracer [72] or thermodynamic [73] techniques.

Our present interest is in stage III where the Pt oxidation is initiated by partial discharging of the adsorbed water molecule to form a oxidized species which needs to be identified. An M_e of 6.1±0.6 g mol^{-1} in stage III is certainly related to the surface-oxide film formation, and possibly change of the adsorption behavior of ion/water. The M_e of 6.1±0.6 g mol^{-1} determined for stage III is supportive of formation of $\mathrm{Pt_2O}$ (8 g mol^{-1}) rather than PtOH (17 g mol^{-1}). However, if the initial oxidation is accompanied by the desorption of previously adsorbed bisulfate [74], both initial species are consistent with the data:

$$\mathrm{2Pt + H_2O} \rightarrow \mathrm{Pt_2O + 2H^+ + 2e^-},\ 8.0\ \mathrm{g\ mol^{-1}} \tag{4.13}$$

$$\mathrm{Pt + H_2O} \rightarrow \mathrm{PtOH + H^+ + e^-},\ 17.0\ \mathrm{g\ mol^{-1}} \tag{4.14}$$

$$\mathrm{Pt(HSO_4)}_x + (x\text{-}x')\mathrm{e^-} \rightarrow \mathrm{Pt(HSO_4)}_{x'} + (x\text{-}x')\mathrm{HSO_4^-},\ -97(x\text{-}x')\ \mathrm{g\ mol^{-1}} \tag{4.15}$$

Shimazu obtained almost the same molar mass per electron of 5.9 g mol^{-1} for stage III with correction for double layer effects, but concluded that the initial species was still PtOH, provided that the "sum of M_e" for stages I-III matches that of OH [75]. Interestingly, Jerkiewicz refrained from calculation of the M_e for the single stage III, but obtained a M_e of 15.8 g mol^{-1} for an extended stage from "potential of zero total charge" (ca. 0.27 V) to 1.40 V. Such results agreed with his proposed Pt_2O species in the early stage [66].

In stage IV, the initially-formed surface oxide is further oxidized to a higher oxidation state for Pt (II, IV...). An M_e of 9.1±0.9 g mol^{-1} determined for stage IV is apparently caused by the incorporation of oxygen into the initial oxide lattice and the number of coordinated oxygen to Pt may increase correspondingly. And this result undoubtedly supports the formation of PtO from Pt_2O, but hardly from PtOH, as first pointed out by Birss et al. [64]:

$$\mathrm{Pt_2O + H_2O} \rightarrow \mathrm{2PtO + 2H^+ + 2e^-},\ 8.0\ \mathrm{g\ mol^{-1}} \tag{4.16}$$

$$\mathrm{PtOH} \rightarrow \mathrm{PtO + H^+ + e^-},\ -1\ \mathrm{g\ mol^{-1}} \tag{4.17}$$

This result implies that the initially formed oxide species is Pt_2O.

4.7 Discussion

The idea of probing the free Pt coverage in the initial stage of Pt oxide formation with molecules such as H_2 and O_2 was found to be a simple and reliable way to study the initial oxide formation. One important assumption is that the active current component (j_ox or j_red) can be directly calculated by removing the baseline current from the solution saturated with probe molecules. The validity of this assumption requires that the reaction cosuming the probe molecules on the Pt surface doesn't affect the Pt surface conditions and the oxide growth, so that the CV baseline current remains unchanged. Although the active current component is sensitive to the availability of the uncovered Pt sites, the actual coverage by the adsorbed probe molecule is infinitesimal. For a diffusion-limited current, the current density still depends on the product of rate constant and surface concentration. For a first-order reaction:

$$j_{\mathrm{l}} = \frac{nFDC^{*}}{\delta} = nFkC_{\mathrm{s}} \tag{4.18}$$

where j_{l} is the limiting current, k is the rate constant of rate-determing step and C_{s} is the surface concentration of adsorbed intermediate. For most reasonable mechanisms, when sufficient overpotential is incurred to make the electron transfer rate infinitely large, the surface concentration will shrink to be infinitesimal to maintain the constant limiting current. The adsorbed probe molecule is unlikely to affect other concurrent surface processes at a infinitesimal surface concentration and therefore infinitesimal surface coverage, unless it is a direct reactant in another process, e.g., the adsorbed oxygen molecule may contribute to the initial Pt oxidation.

The comparison of frequency response in the solution with and without probe molecules also shows little effect of the presence of these molecules (Fig. 4.15). Careful frequency analysis found the three frequency curves are nearly identical in: the H_2 UPD region, the double layer region, the surface oxidation formation/stripping region and the maximum frequency change for a positive- or negative-going sweep. This implies that the double layer and surface structure was unaffected, even though these molecules are introduced into solution and result in additional reaction at the Pt-solution interface.

The above methods allow direct determination of the oxide film coverage on Pt from the net H_2 oxidation current j_{ox}, assuming that the decrease in j_{ox} is mainly due to the gradual covering of fresh Pt sites by the oxide film. Some researchers [76, 77] observed that H_2 oxidation current begins to decrease at potentials much less (e.g. < 0.45 V) than the onset potential of Pt oxidation, and ascribed the decrease in j_{ox}

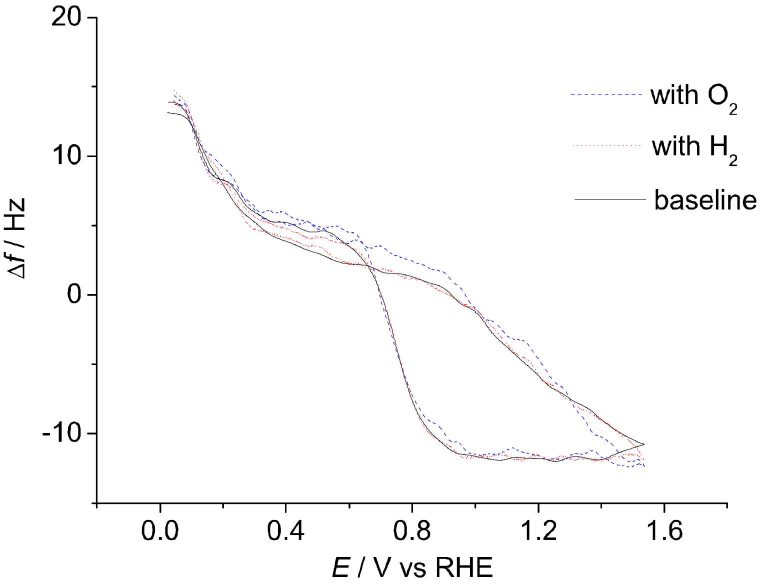

Figure 4.15: Comparison of frequency response by a single potential cycle in 0.5 M H_2SO_4 saturated by H_2 or O_2, sweep rate at 20 mV s^{-1}.

in the initial stage of Pt oxidation to anion adsorption. The anion adsorption must be a minor concurrent process during the initial oxidation of the Pt surface, because the amount of adsorbed anions required for complete inhibition of HOR would cause sufficient mass accumulation to be detected by EQCM, but we didn't find any such result in our EQCM experiments. Recently Bao and Macdonald [78] interpreted the small residual H_2 oxidation current on oxide film with a tunneling current theory, and further concluded that the decrease in oxidation current is due to the thickening of a uniform oxide film. They obtained results on oxide films with estimated thicknesses of 0.1–1 nm. Thicknesses of 0.1 nm seem unrealistic for uniform barrier films, and we prefer a more molecular level chemisorption picture.

The method discussed above provides a reliable definition of the initial stage of Pt oxidation. The oxidation of the Pt surface is triggered at 0.85 V, and the initially-free Pt surface atoms are gradually oxidized to a certain oxidation state (I, II or higher), and bonded to oxygen-containing species (OH^-, O^{2-}, etc.). The point where each Pt atom is oxidized marks the end of the initial stage, usually at a critical potential of 1.15 V, where many electrochemical processes catalyzed by Pt surface (HOR, ORR, etc.) are also significantly suppressed. The charge analysis suggested one electron oxidation for per Pt occurs in the early stage, and such result conforms with the formation of uniform surface P(I) species and other surface structure such as every second surface Pt atom as Pt(II) species.

The composition of the initial oxidation species has been suggested to be a hydrous Pt-OH, formed by partial discharge of adsorbed water molecule [49], or a bridging oxygen species (Pt_2O), formed by complete discharging of water molecule with the O residing between two adjacent surface Pt atoms [66]. The model of forming PtOH species and its further oxidation as originally suggested by Conway is described by the following reactions [65]:

$$\mathrm{Pt} + \mathrm{H_2O} \rightarrow \mathrm{Pt\text{-}OH(ads)} + \mathrm{H^+} + \mathrm{e^-};\ 0.85\text{-}1.10\ \mathrm{V} \tag{4.19}$$

$$\mathrm{Pt\text{-}OH(ads)} \rightarrow \mathrm{Pt\text{-}O} + \mathrm{H^+} + \mathrm{e^-};\ 1.10\text{-}1.40\ \mathrm{V} \tag{4.20}$$

$$\mathrm{Pt\text{-}O} \rightarrow \mathrm{O\text{-}Pt};\ \text{place-exchange} \tag{4.21}$$

And the model of forming bridging Pt_2O given by Jerkiewicz is shown as follows [66]:

$$\mathrm{Pt} + \mathrm{H_2O} \rightarrow \mathrm{Pt^{\delta^+}\text{-}(O^{\delta^-}H_2)_{physi}};\ 0.27\text{-}0.85\ \mathrm{V} \tag{4.22}$$

$$\mathrm{(Pt\text{-}Pt)\text{-}H_2O} \rightarrow \mathrm{(Pt\text{-}Pt)^{\delta^+}} - \mathrm{O^{\delta^-}} + 2\mathrm{H^+} + 2\mathrm{e^-};\ 0.85\text{-}1.15\ \mathrm{V} \tag{4.23}$$

$$\mathrm{Pt\text{-}O} + \mathrm{H_2O} \rightarrow \mathrm{(Pt^{2+}\text{-}O^{2-})_{quasi\text{-}3D\ lattice}} + 2\mathrm{H^+} + 2\mathrm{e^-};1.15\text{-}1.40\ \mathrm{V} \tag{4.24}$$

These two mechanisms are both consistent with the fact that the charge involved in the initial stage indicates oxidation to the extent of one electron per Pt. In contrast, Harrington [46] proposed a single step oxidation mechanism for the overall stage of Pt oxidation and showed only Pt(II) species was formed in the early stage. The validity of this mechanism will require a surface structure with mixed Pt atoms and Pt(II) species, but such structure may not be as stable as uniform surface Pt(I) species.

The EQCM results indicated that a surface species with Pt_2O stoichiometry was formed in the early stage. Such species could have the structure with O^{2-} sitting between two ajacent surface Pt atoms, as suggested by Jerkiewicz, but could have other structures. It is noteworthy that although the composition of the initial oxidation species was proposed to be PtOH in the very early days and thoroughly investigated, the proposition of Pt_2O has been favorably supported by EQCM studies done by many different researchers, including our work.

4.8 Conclusions

A convenient methodology was developed to use simple molecules to probe free surface sites in the early stage of Pt oxide formation. H_2 is an ideal probe molecule that shows an oxidation current proportional to the fraction of the surface covered by free sites. This oxidation current helps to identify the onset potential of Pt oxidation as 0.85 V, as well as the finishing potential of the initial stage of oxidation at 1.15 V. The RDE experiment is an important modification to ensure controlled convection. The O_2 was tested as alternative probe molecule but is not as suitable as H_2 due to its pronounced interference with the oxide growth. The mass response by EQCM confirmed the initially-formed species to have a Pt_2O stoichiometry.

Chapter 5

Ag promoted Pt dissolution

5.1 Introduction

The electrochemical stability of Pt electrodes, with respect to dissolution into the electrolyte, particularly in non-complexing acids has long been investigated. Tafel [79] first mentioned the dissolution of Pt electrodes by repetitive oxidation and reduction cycles in acidic media. Later a few authors pointed out that the Pt electrode may dissolve even under mild anodic conditions [80–82]. The immediate evidence for Pt dissolution was from the imbalance between the anodic charge for Pt oxidation (Q_a) and cathodic charge required for complete reduction of oxide (Q_c) in potential cycling [4, 83]. Some investigators ascribed the larger anodic charge than cathodic charge (as much as twice) to the formation of oxide film which was not completely reduced in the cathodic cycle, i.e., a portion of the oxide film was chemically dissolved in acid [84–86]. Such a substantial charge imbalance, in contrast, was suggested by Gilman to be caused by oxidation of adsorbed impurities or improper correction for double layer charging [4].

Direct evidence for Pt dissolution and its possible causes have been sought in many different ways. Biegler investigated the activation and roughening of Pt electrodes during potential cycling in sulfuric acid, and based on his electron microscopy analysis, demonstrated that when the surface Pt atoms are coordinated with more than one oxygen per Pt in the anodic cycle and then reduced in a fast cathodic cycle, the rearrangement of Pt surface atoms and dissolution of surface oxide species occurs [87]. Johnson et al. detected soluble Pt species on the ring electrode during both oxidation and reduction cycles on the disk electrode in their rotating ring disk electrode (RRDE) experiments, in both sulfuric and perchloric acids. The Pt species produced during the reduction of Pt oxide was identified as Pt(II) by spectrophotometry, while the species in the oxidation cycle remained unindentified [88]. Following these works, Rand et al. carefully analyzed the amount of dissolved Pt in solution by atomic absorption spectroscopy and compared with the imbalanced charge, and claimed instead that the soluble species was Pt(IV) and not Pt(II) [89]. Their results also showed that the Pt electrode dissolves only when a critical anodic potential limit of 1.07 V (RHE) is exceeded. Untereker [90] repeated the RRDE experiments and detected soluble Pt species during both cathodic and anodic cycles, in good agreement with Johnson's results. Furthermore, by observing a decreased roughening rate at higher rotation rate, the author concluded that the dissolution-redeposition process was the major cause for surface roughening.

The anodic mechanism proposed to explain the Pt dissolution, involves either the direct dissolution of Pt from the metal phase,

$$\mathrm{Pt} \rightarrow \mathrm{Pt}^{2+} + 2\mathrm{e}^- \tag{5.1}$$

or dissolution of some intermediate surface oxide species,

$$\begin{aligned} \mathrm{Pt} + x\mathrm{H_2O} &\longrightarrow \mathrm{PtO}_x + 2x\mathrm{H}^+ + 2x\mathrm{e}^-,\ x = 1 \text{ or } 2 && (5.2)\\ \mathrm{PtO}_x + 2x\mathrm{H}^+ &\longrightarrow \mathrm{Pt}^{2x+} + x\mathrm{H_2O} && (5.3) \end{aligned}$$

The anodic mechanism is mostly applicable for the Pt dissolution under galvanostatic

[91] or potentiostatic [92–94] conditions, as has been carefully examined in the fuel cell industry. There is increasing evidence of the anodic-cathodic mechanism, which requires the reduction cycle of Pt oxide film. In the anodic cycle, the surface oxide is supposed to undergo "place-exchange", in which there is vertical motion of Pt atoms out of the metallic phase and movement of oxygen underneath the Pt atoms. The place-exchange is driven by the "dipole-dipole lateral repulsive interactions" and occurs at an onset potential of ca. 1.15 V [66]. Upon reduction, the place-exchanged Pt atoms don't return to their original lattice position, but remain on the surface as high energy Pt atoms with weakened bonding to underlying Pt sites, resulting in a roughened surface structure with islands, shallow pits, etc., which are detectable by X-ray scattering [95], in situ STM [96], and spot shape variations in LEED analysis [97]. Some of these Pt atoms, or Pt-oxygen species are attacked by acid and dissolve into the solution. According to the anodic-cathodic mechanism, the "place-exchange" is the critical process for both Pt surface roughening and dissolution in oxidation-reduction cycles.

When Pt electrodes are used as a substrate for metal (in our case, Ag) deposition, the oxidation and reduction reactions of the Pt surface are concurrent with the metal deposition and stripping reactions. It is known that underpotentially deposited Ag monolayers on the Pt surface (both single and polycrystalline) preferentially undergo place exchange to form a surface alloy prior to the multilayer deposition of a thicker Ag layer [98–104]. This alloying process takes place via the surface reordering of Ag-Ag, Ag-Pt and Pt-Pt domains to reduce the surface stress. We show here that there is much greater Pt dissolution from repetitive Ag deposition-stripping cycles on the Pt surface than from the oxidation-reduction cycles of the Pt surface itself. Evidence comes from the persistent frequency drift for each potential cycle and the monitored Pt concentration change in solution measured by the ICP-MS technique. A significant change in roughness and electrocatalytic properties of Pt surfaces was also observed. We propose a mechanism suggesting that the Pt-Ag alloying and dispersed Pt surface atoms produced in anodic stripping account for the observed Pt dissolution.

5.2 Electrodeposition and stripping of Ag on Pt

Against a Ag|Ag$^+$ reference electrode, the reversible potential for Ag electrodeposition sits at 0.0 V. Underpotential deposition (UPD) occurs when the metal-substrate bonding is stronger than the metal-metal bonding, and the UPD peak is located at a more positive potential than the reversible potential. In the negative-going potential sweep, the Ag UPD begins at 0.3 V and reaches a peak current at 0.1 V (peak c1 in Fig. 5.1a). During UPD deposition, the first monolayers of Ag are deposited onto the Pt electrode surface, and they act as substrates for the following Ag overpotential deposition (OPD) where multilayers of Ag are deposited. The OPD begins at ca. 0 V, immediately following the UPD, which suggests that the OPD Ag atoms are deposited onto a "genuine" Ag electrode which is the Pt electrode completely covered by an Ag film with bulk-like structure. The Ag OPD reaches a peak current at –0.1 V (peak c2). The UPD and OPD processes are represented by the following equations:

$$\mathrm{Pt} + \mathrm{Ag}^+ + \mathrm{e}^- \rightarrow \mathrm{PtAg(ads)};\ \mathrm{UPD},\ E_\mathrm{p} = 0.1\ \mathrm{V} \tag{5.4}$$

$$\mathrm{Ag}^+ + \mathrm{e}^- \rightarrow \mathrm{Ag};\ \mathrm{OPD},\ E_\mathrm{p} = -0.1\ \mathrm{V} \tag{5.5}$$

The different peak potentials of UPD and OPD are reflective of different bonding energies between Ag-Pt and Ag-Ag. However, only at low concentrations (1 mM or less) and low sweep rates (200 mV or less) are the UPD and OPD peaks well separated, as observed during Ag deposition in a 1 mM $\mathrm{AgClO_4}$ solution (see Fig. 5.1a). Continuing the negative-going sweep, the Ag deposition becomes completely controlled by diffusion and shows a flat current in region c3. The Pt-catalyzed hydrogen underpotential desorption is inhibited when Ag layers are present on the Pt surface, and no characteristic hydrogen UPD peaks are observed in region c3 (equivalent to 0-0.2 V vs. RHE). At $E < –0.6$ V vs. Ag|Ag$^+$, the cathodic current begins to drop sharply due to H_2 evolution. In the positive-going sweep, the Ag continues to deposit at $E < 0$ V until it reaches a sharp anodic stripping peak at $E_\mathrm{p} = 0.05$ V (peak a1). The stripping peak a1 strips most deposited Ag layers from the Pt surface, and the last few layers of Ag are stripped during peak a2 and a3. When the potential is swept to higher potentials up to the anodic potential limit at 0.9 V (1.5 V vs. RHE), the oxide thin film develops on the bare Pt surface.

A large frequency shift was observed when adding and removing heavy Ag atoms (see Fig. 5.1b). The 9 MHz quartz crystal has a calibration constant of 0.188 Hz ng^{-1} cm^2, which gives 1.0 Hz frequency shift per 5.32 ng cm^{-2} deposit. Assuming the monolayer charge of 205 μC cm^{-2} per Pt for Ag (Ag atom is slightly larger than Pt, ca. 4% in radius), each monolayer of Ag onto Pt electrode causes a 43.0 Hz frequency drop. A 60.5 Hz frequency change in the UPD region shows that ca. 1.4 monolayers of Ag are underpotentially deposited onto the Pt surface, and the maximum frequency drop of 940.2 Hz shows that a total of 21.9 monolayers of Ag are deposited onto Pt surface before the stripping occurs. The simultaneously monitored frequency was plotted against charge density for the negative- and positive-going sweep, and the molar mass per electron (M_e) was calculated according to Eq. (4.10), as shown in Fig. 5.2. It was found that only for the diffusion-controlled deposition (c3) and stripping of bulk Ag (a1) was the determined M_e of 109 g mol^{-1} close to the ideal molar mass 107.9 g mol^{-1} for Ag. The M_e is determined to be 39.4 g mol^{-1} in the UPD region and 95.9 g mol^{-1} in the OPD region. The deviation from ideal molar mass of Ag is attributed to many effects, such as surface roughness changes during deposition and adsorption/desorption of water molecules. Detailed results and discussion can be found in earlier work from our group [8].

The large deviation from ideal molar mass of Ag in the UPD region can readily be explained by the superimposed reduction reaction of Pt surface oxide. It has been reported that the Ag deposition is completely inhibited by formation of a full oxide

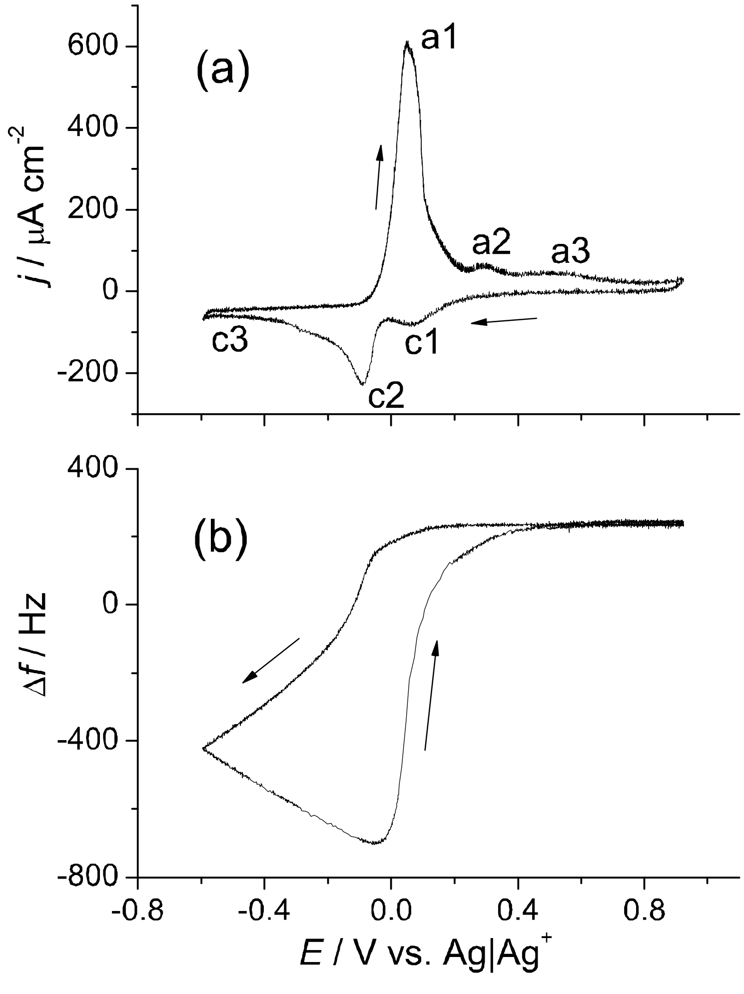

Figure 5.1: Pt cyclic voltamogram in 1 mM $AgClO_4$, and simultaneous EQCM frequency response. 20 mV s^{-1}, versus Ag^+|Ag reference electrode.

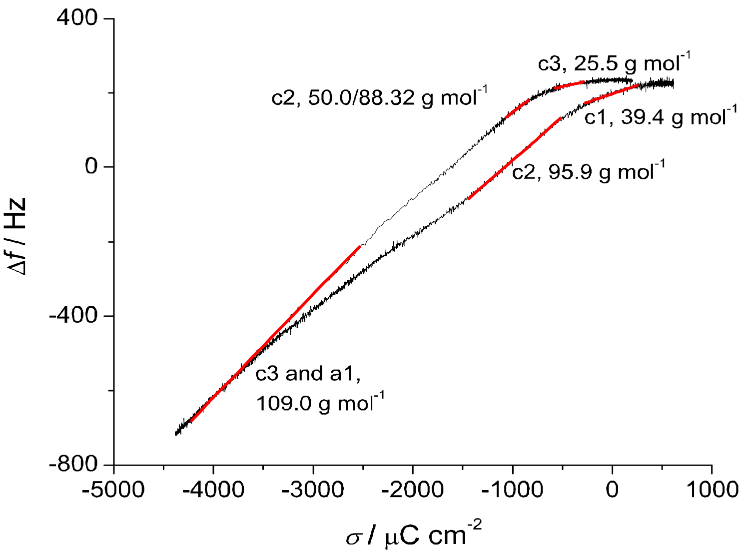

Figure 5.2: The frequency-charge density analysis for silver deposition onto Pt electrode. 1 mM $AgClO_4$, sweep rate 20 mV s^{-1}.

layer [105,106]. Therefore it is clear that in the Ag UPD region, the Ag only deposits on fresh Pt sites released from the reduction of the Pt oxide, as described by the following equation:

$$PtO_x + yAg^+ + 2xH^+ + (2x + y)e^- \rightarrow PtAg_y(ads) + xH_2O \qquad (5.6)$$

The overall process gives a M_e of $(108y\text{-}16x)/(2x{+}y)$ g mol^{-1}. The determined M_e of 39.4 g mol^{-1} for overall Ag UPD region is in excellent agreement with the complete reduction of PtO species ($x = 1$) followed by deposition of 1.4 monolayers ($y = 1.4$) of Ag, which gives 39.8 g mol^{-1}. Further evidence for mixed Pt oxide reduction with Ag UPD can be found by comparing CVs of these two reactions in Fig. 5.3 (The potentials versus the RHE measured in $HClO_4$ solutions have been converted to those versus the Ag|Ag$^+$ reference electrode). At both the high and low sweep rates, the onset potential for Ag UPD is located at 0.35 V, where Pt oxide begins to be

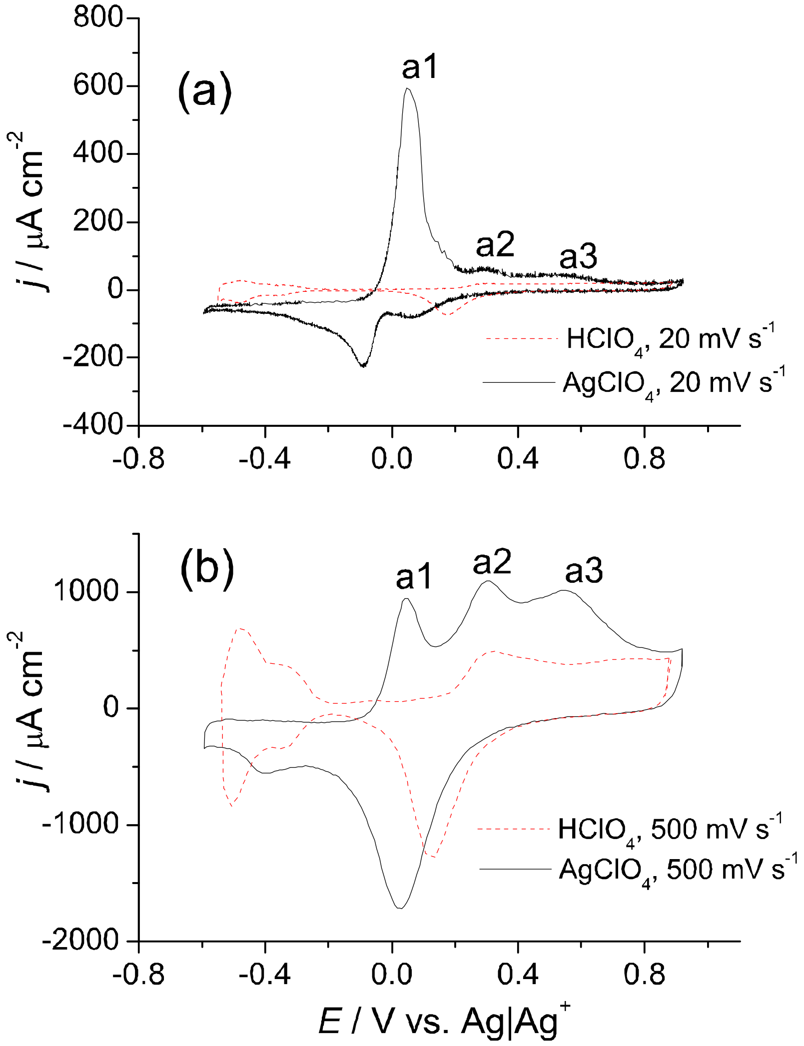

Figure 5.3: Comparison of the voltammograms in $AgClO_4$ and $HClO_4$ solutions. Sweep rate: (a) 20 mV s^{-1}; (b) 500 mV s^{-1}.

Table 5.1: Number of monolayers for anodic stripping peaks a1, a2 and a3, calculated according to charge density. The figures in parentheses refer to those calculated according to the EQCM frequency shift

number of monolayers	a1	a2	a3
20 mV s^{-1}	16.2	1.9	3.3(0.62)
500 mV s^{-1}	1.1	2.3	3.3(0.07)

reduced. The single UPD peak suggests that the reaction rate for Ag UPD is faster than the rate for oxide reduction.

The stripping voltammograms have three distinctive stripping peaks located at different potentials: 0.05 V (a1), 0.30 V (a2) and 0.55 V (a3), corresponding to three different Ag bonding energies and multilayer structures (see Fig. 5.3). For the low sweep rate of 20 mV s^{-1}, the first stripping peak (a1) has a much higher peak current and total charge than for peaks a2 and a3. This shows that at low sweep rates most Ag multilayers are deposited overpotentially and stripped around the reversible potential. However for the high sweep rate of 500 mV s^{-1}, the peaks a2 and a3 have comparable or even higher charges than the first stripping peak a1. This shows that the three different Ag multilayer structures formed at high sweep rate are of comparable amounts. The charge density was calculated by integrating the current for each anodic stripping peak, and is listed in Table 5.1.

The number of monolayers of peak a3 can't be determined accurately, because the removal of the last monolayer of Ag overlaps with Pt oxide formation. Fortunately, the much lower molar mass of oxygen atoms compared with Ag atoms makes the EQCM frequency analysis more reliable than the charge analysis. The total frequency shift for region c3 was determined to be equivalent to 0.63 monolayers for peak a3 at 20 mV s^{-1} and 0.07 monolayers at 500 mV s^{-1}, respectively. The representative structures of the Ag multilayers deposited on bare Pt substrate are shown schematically in Fig. 5.4. The first structure is the Pt-Ag alloy, formed first in the negative-going cycle, and stripped as peak a3 at the very end of the stripping cycle. The growth of the

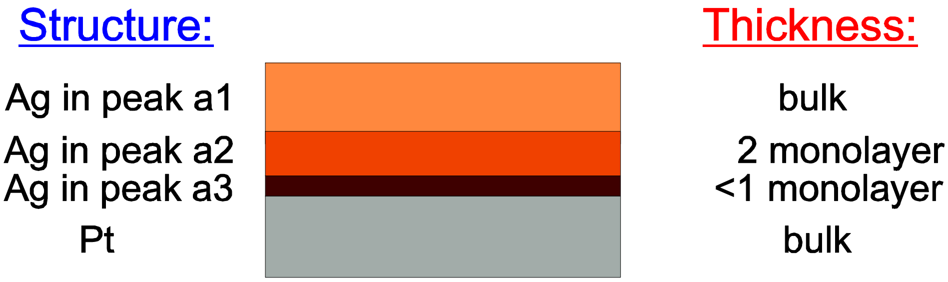

Figure 5.4: Schematic of three different Ag multilayer structures on the Pt electrode, deposited in the negative-going sweep.

Pt-Ag alloy apparently depends on time, as is evident from the different thicknesses at different sweep rates. Vaskevich observed formation of Pt-Ag alloy on a time scale of a few minutes [104], and other researchers found that the Ag-Pt alloy formation was promoted by long-time cycling [101] or cathodization, i.e., held at constant reductive current [98]. The next two monolayers of Ag (stripped in peak a2) are deposited on the top of the Ag-Pt alloy, bonded to the underlying Ag and Pt atoms in the alloy lattice. Finally the bulk Ag was always deposited on top of a Ag layer, as represented by peak a1. Different anodic peak potentials were the result of different bonding conditions for different multilayer structures.

5.3 Frequency drift phenomena

The Pt cyclic voltammetry and frequency response for pure 0.5 M $HClO_4$ is shown in Fig. 5.5. The frequency quickly drops when the potential sweeps into the Pt surface oxide formation region ($E > 0.80$ V). The frequency plateaus after the potential reversal at $E = 1.55$ V vs. RHE; the hysteresis shows the irreversible nature of the formation and reduction of the Pt oxide. The frequency resumes the positive-going behaviour when the potential sweeps negatively into the double layer region. The rather large frequency change in the hydrogen UPD region is due to water adsorption/desorption or by the hydrophobic/hydrophilic property change of the Pt

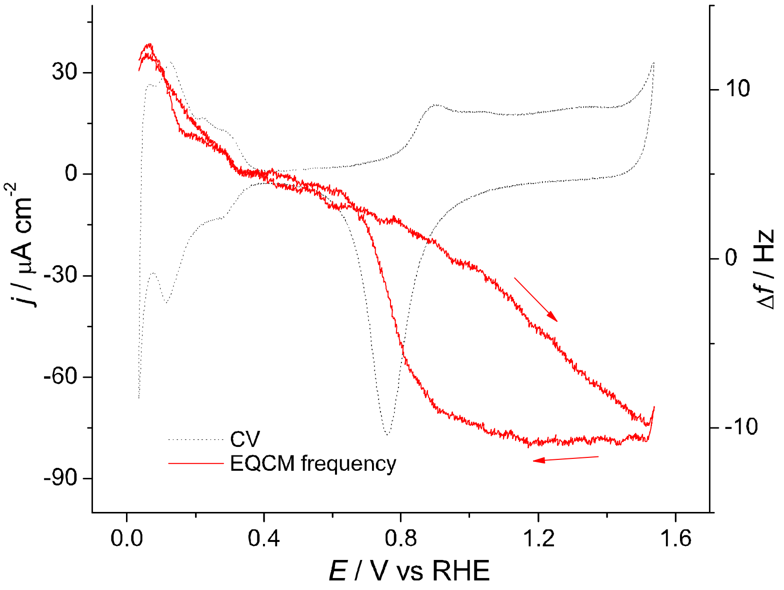

Figure 5.5: The Pt cyclic voltammogram in 0.5 M $HClO_4$ solution (dashed trace) and simultaneous frequency response (solid trace), 20 mV s^{-1}.

surface [107]. For each complete cycle, the frequency response showed a close loop. Continuous and successive cycling showed very little frequency drift (60 Hz over 6 hours, see Fig. 5.6), which was about the same magnitude as the instrumental drift and system instability. Experiments were repeated at a higher sweep rate of 200 mV s^{-1} and with heated solution (40-60 °C), but there was still no measurable frequency drift. Thus our mirror polished Pt electrode on quartz crystal proved to be inert in 0.5 M $HClO_4$.

When 1 mM $AgClO_4$ solution was added into the 0.5 M $HClO_4$ solution, the characteristic voltammetry and frequency features for Ag deposition and stripping were observed. Both the current transient and the frequency response were recorded simultaneously, as presented in Fig. 5.7. The most interesting feature is that for each complete cycle, the frequency response doesn't form a closed loop. Instead a frequency drift of +8.3 Hz was observed for each cycle and this steady frequency drift persisted

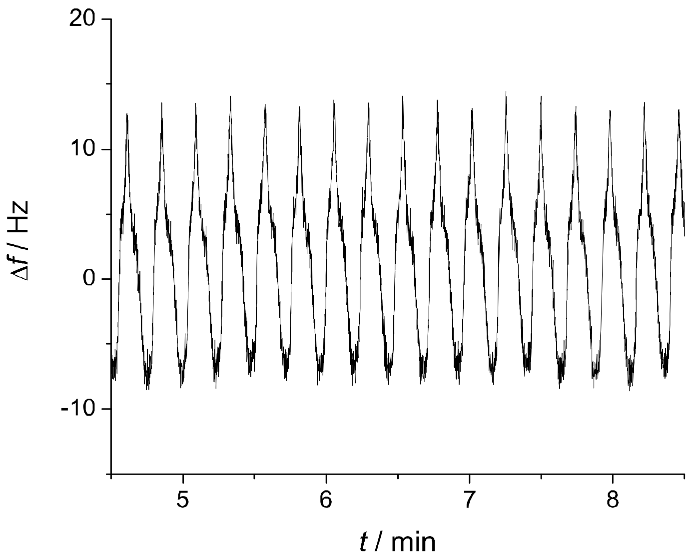

Figure 5.6: The frequency response during successive cycling in 0.5 M $HClO_4$. Sweep rate 200 mV s^{-1}, -0.05 V to 1.55 V vs. RHE.

in successive cycling for as long as 11 hours (see Fig. 5.8). A variety of property changes at the electrode-liquid interface give frequency drift, as discussed in Chapter 3, but few of them give persistent and substantial frequency drifts. This characteristic frequency drift appeared to be caused by mass loss due to Pt dissolution from the working electrode, and therefore we sought to confirm this with further experiments.

5.4 ICP-MS analysis of Pt dissolution

To test the Pt dissolution over a long time scale, extended potential cycling (>10 hours) was performed in 0.5 $HClO_4$ solution with and without 1 mM $AgClO_4$ solution, at a sweep rate of 200 mV s^{-1}. The base $HClO_4$ solution was cycled for 12 hours, either with or without Pt oxide formation, i.e., potential range from 0.05 V to 0.75

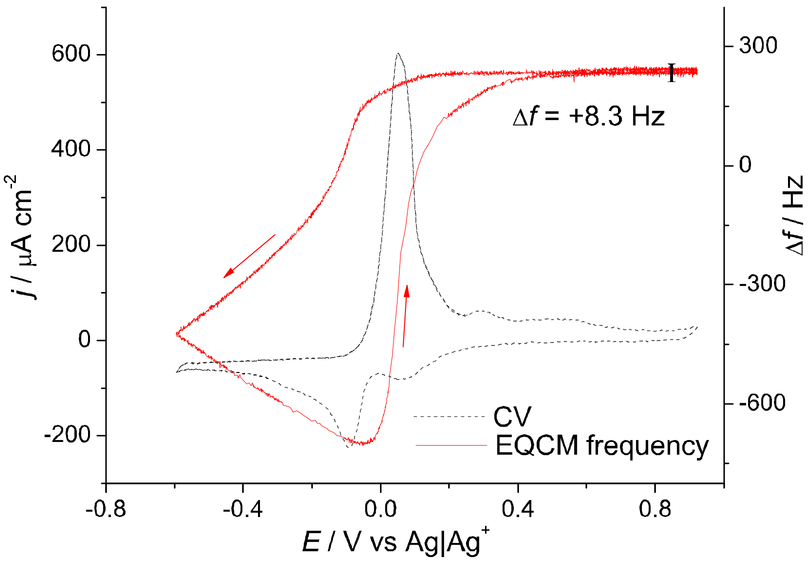

Figure 5.7: The Pt cyclic voltammogram in 1 mM $AgClO_4$ solution (dashed trace) and simultaneous frequency response (solid trace), 20 mV s^{-1}, –0.6 V to 0.9 V vs. $Ag|Ag^+$.

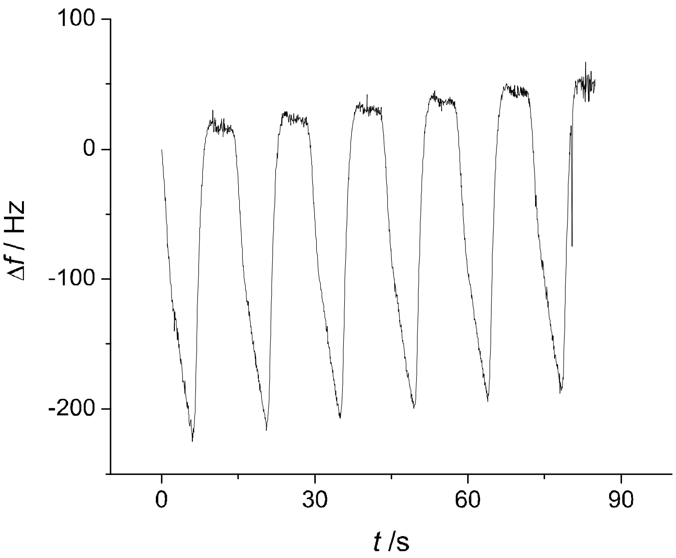

Figure 5.8: The frequecy drift for repeated cycling in 1 mM $AgClO_4$ + 0.5 M $HClO_4$, 200 mV s^{-1}, -0.6 V to 0.85 V vs. Ag|Ag^+.

V (treatment I) and 0.05 V to 1.5 V vs. RHE (treatment II). Similar experiments were performed in the presence of 1 mM $AgClO_4$ by controlling the potential between -0.6 V to 0.25 V (treatment III) and -0.6 to 0.85 V vs. Ag|Ag^+ (treatment IV). The anodic potential limit of 0.25 V vs. Ag|Ag^+ (0.85 V vs. RHE) for treatment III was deliberately chosen to avoid Pt oxidation and to ensure that the last monolayer of Ag was always stripped in each cycle so that no Ag mass is accumulated during the long experiment. The frequency response was recorded simultaneously and the total frequency drift Δf was used to calculate the total mass of dissolved Pt and therefore the molar concentration of Pt ([Pt]) in solution, assuming all the frequency drift was due to the loss of Pt material from the electrode surface. The solutions were then tested by ICP-MS for the actual Pt concentration in solution with ppb accuracy. The following table 5.2 compares the obtained [Pt] from EQCM frequency measurements and ICP-MS tests.

Table 5.2: Pt concentration in solution detected by ICP-MS and EQCM. Figures in parentheses refer to total frequency drift.

[Pt] / mol L^{-1}	$HClO_4$ blank	I	II	III	IV
by ICP-MS	$< 5\times10^{-8}$	$< 5\times10^{-8}$	$< 5\times10^{-8}$	1.5×10^{-7}	2.1×10^{-6}
by EQCM	-	-1.9×10^{-9} (-17 Hz)	3.2×10^{-8} (286 Hz)	1.5×10^{-8} (133 Hz)	2.2×10^{-6} (19635 Hz)

ICP-MS results showed no detectable [Pt] in both types of potential cycled $HClO_4$ solutions (I and II) and the frequency response corresponded to [Pt] comparable or less than the detection limit. A noticeable +286 Hz drift, corresponding to dissolution of 3.7 ML of Pt was measured for cycling between 0.05 and 1.5 V vs. RHE in $HClO_4$. The inferred [Pt] of 3.2×10^{-8} mol L^{-1} was just below the detection limit of ICP-MS, but is likely significant, given the accuracy of the other data. Thus the EQCM accurately measures the frequency change and has better sensitivity than ICP-MS for detection of dissolution.

Substantial Pt dissolution was detected in potential cycled $AgClO_4$ solution where Ag was repeatedly deposited and stripped. A large frequency drift of 19635 Hz was observed by cycling over the full range from -0.6 V to 0.85 V vs. $Ag|Ag^+$, corresponding to a [Pt] $= 2.2\times10^{-6}$ mol L^{-1}. This result closely matches the concentration of 2.1×10^{-6} mol L^{-1} detected by ICP-MS, confirming that the Pt dissolution from the working electrode is the main source of frequency drift, and more importantly that the monitored long-term frequency drift during potential cycling is capable of directly indicating Pt dissolution. A discrepancy was found for treatment III: ICP-MS gave a noticeable [Pt] $= 1.5\times10^{-7}$ mol L^{-1}, which would correspond to a frequency drift of +623 Hz. However a smaller frequency drift of +133 Hz was measured, suggesting inaccuracy of ICP-MS in detecting the extremely low Pt concentration, since a concentration of 1.5×10^{-7} mol L^{-1} is only three times above the detection limit.

Ag deposition and stripping on the counter electrode (CE) may lead to enhanced CE dissolution that interferes with the comparison of the EQCM and ICP-MS dissolution rates. The CE has a 25 times larger surface area (5.72 cm^2) than the working

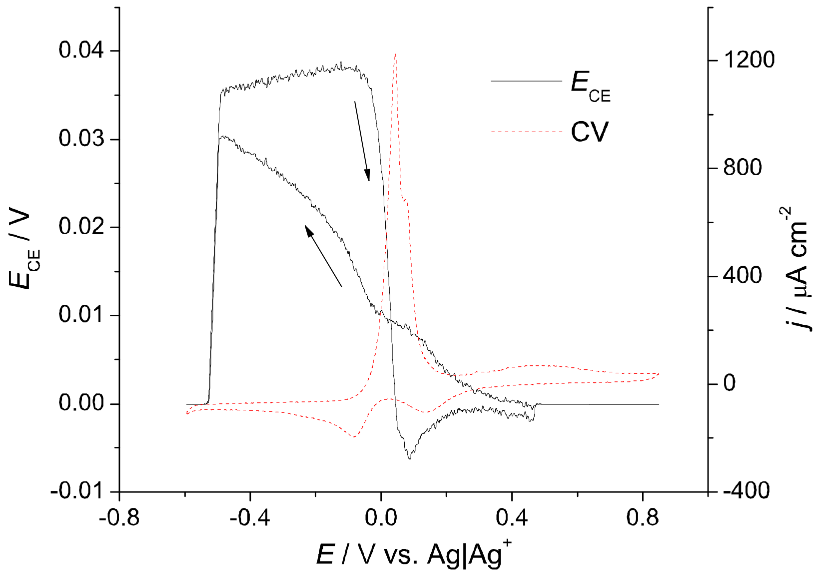

Figure 5.9: The monitored electrode potential of Pt counter electrode ($A = 5.72$ cm^2) during potential cycling on Pt working electrode in 1 mM $AgClO_4$. Potential range –0.6 to 0.85 V vs. Ag|Ag$^+$, sweep rate 20 mV s^{-1}.

electrode. To study the effect of the CE, its potential was monitored during the controlled Ag deposition and stripping on the WE, as shown in Fig. 5.9. The potential of the CE was found to be close to the reversal potential for Ag electrodeposition, 0.02±0.025 V vs. Ag|Ag$^+$ during potential cycling on the WE. The CE did not experience the UPD to OPD transition when the Ag is anodically stripped from WE, but dynamic deposition and stripping of a very small amount of Ag (less than 1 ML) does take place on its surface. The dissolution of Pt apparently requires growth of Pt-Ag alloy under cathodic conditions followed by stripping of the alloyed Ag at anodic overpotential ($E > 0.43$ V vs. Ag|Ag$^+$). Therefore the conditions at the CE during potential cycling of the WE are unfavorable for Pt dissolution from the CE, and therefore do not degrade the good agreement between the Pt concentrations detected by ICP-MS and EQCM.

5.5 Electrode morphology change resulted from Pt dissolution

Extensive potential cycling in 1 mM $AgClO_4$ causes a large amount of Pt to be lost from the electrode surface, and may lead to a significant change in the properties of the Pt surface. The morphology of the Pt surface before and after the potential cycling was monitored by AFM, as shown in Fig. 5.10. The initial AFM image (Fig. 5.10a) shows the initial polished Pt surface with surface features of $\sim$12 nm height and $\sim$30 nm lateral length. The roughness factor was 1.2 determined by both hydrogen UPD charge measurements and AFM topology measurement software. After extended cycling ($>$ 10 h at 200 mV s^{-1}) in $AgClO_4$ solution, the Pt surface was significantly roughened (Fig. 5.10b). Many nanometer-sized sharp hills and pits were produced and led to a roughness factor of $>$1.6.

5.6 Potential, temperature and sweep rate dependence of Pt dissolution

5.6.1 Potential dependence

The above ICP-MS results clearly show that Pt dissolution during Ag deposition and stripping has a strong dependence on the anodic potential limit (E_{a}). A low E_{a} (treatment III) may not be able to cause any dissolution of Pt, but a high E_{a} (treatment IV) can result in significant Pt dissolution from the electrode. It is possible to determine the critical E_{a}, which is the minimum E_{a} required for the dissolution of Pt electrode, by potential cycling in a series of experiments with different E_{a} and monitoring the Pt dissolution. Since the EQCM frequency drift directly probes the Pt dissolution, the rate of Pt dissolution can be directly calculated from the rate of

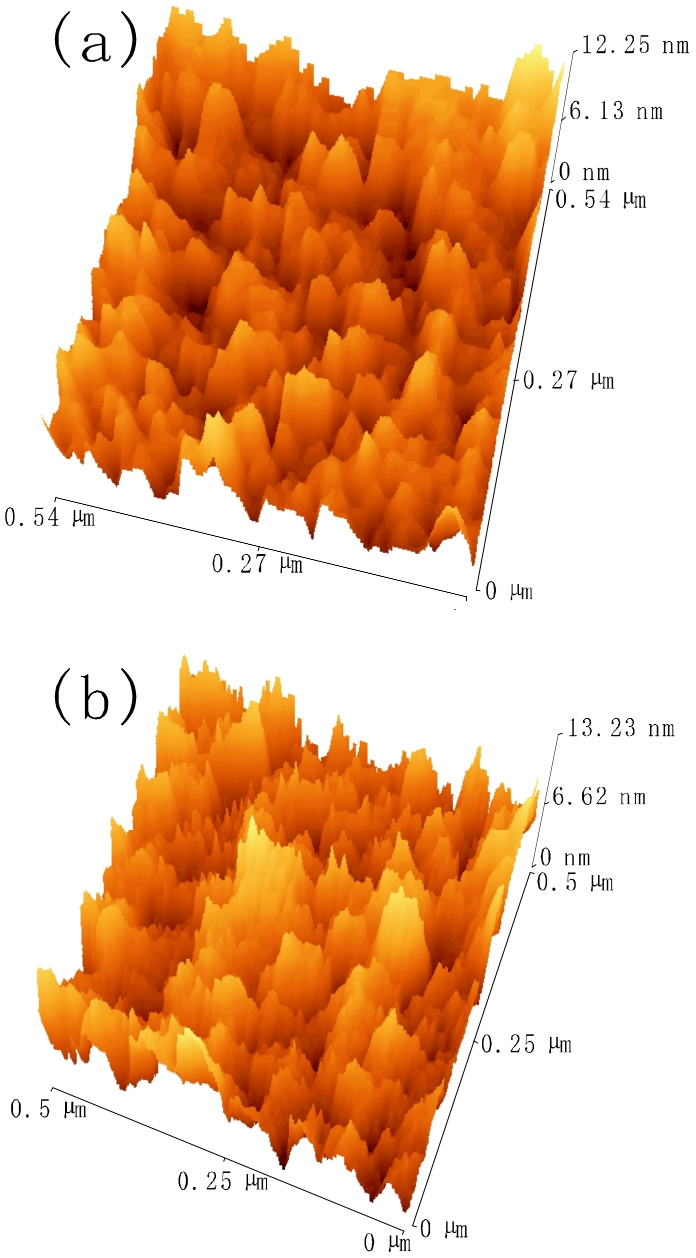

Figure 5.10: Comparison of AFM topographies before and after extended potential cycling in $AgClO_4$ solution. (a) before cycling; (b) after cycling.

frequency drift, e.g., a frequency drift rate of +77.8 Hz cycle^{-1} indicates one monolayer of Pt is lost from the electrode in each potential cycle. The frequency drift rate was determined by linear fitting of the Δf - t curve (e.g., Fig. 5.8) and has units of Hz cycle^{-1} or Hz s^{-1}.

The potential was first cycled between a fixed cathodic potential limit (E_c) at –0.6 V vs. Ag|Ag$^+$ and a variable anodic potential limit (E_a) from 0.40 V to 0.9 V vs. Ag|Ag$^+$, and the frequency drift rate was calculated for each E_a (Fig. 5.11). The frequency drift rate increases almost linearly with the increasing anodic potential limit E_a and has a maximum of 10.5 Hz cycle^{-1} when the anodic limit is controlled at 0.9 V vs. Ag|Ag$^+$. The frequency drift rate at higher anodic potential limits was not obtainable since O_2 evolution occurs on the electrode surface and the bubbles significantly affect the accuracy of the frequency measurement. It was also clearly observed that the frequency drift disappeared when the anodic potential limit was lower than a critical potential of ca. 0.43 V. At even lower anodic potential limits, the frequency drifts negatively per cycle, due to mass accumulation by unstripped Ag layers in each cycle. This critical E_a is located in the rising shoulder of the anodic stripping peak a3 (Fig 5.3a and b), where the alloyed Ag begins to be stripped. Therefore a quick conclusion can be drawn that the repetitive Ag-Pt alloy formation and stripping of alloyed Ag plays an important role in the Pt dissolution.

The influence of the cathodic potential limit on Pt dissolution was also examined. The potential was cycled between a fixed anodic potential limit (E_a) of 0.9 V vs. Ag|Ag$^+$ and a variable cathodic potential limit (E_c) from –0.60 V to –0.2 V vs. Ag|Ag$^+$, and the frequency drift rate was calculated for each E_c (see Fig. 5.12). When the cathodic potential limit (E_c) is increased from –0.6 V to –0.2 V, the frequency drift rate decreases steadily to 5.1 Hz cycle^{-1}, nearly half of the maximum drift rate at E_c = –0.6 V. This is an interesting result since the Ag UPD peak and its paired stripping peak a3 remains nearly unchanged (Fig. 5.12b) at different E_c, showing constant conditions for Pt-Ag alloy formation and stripping. However, the time allowed for

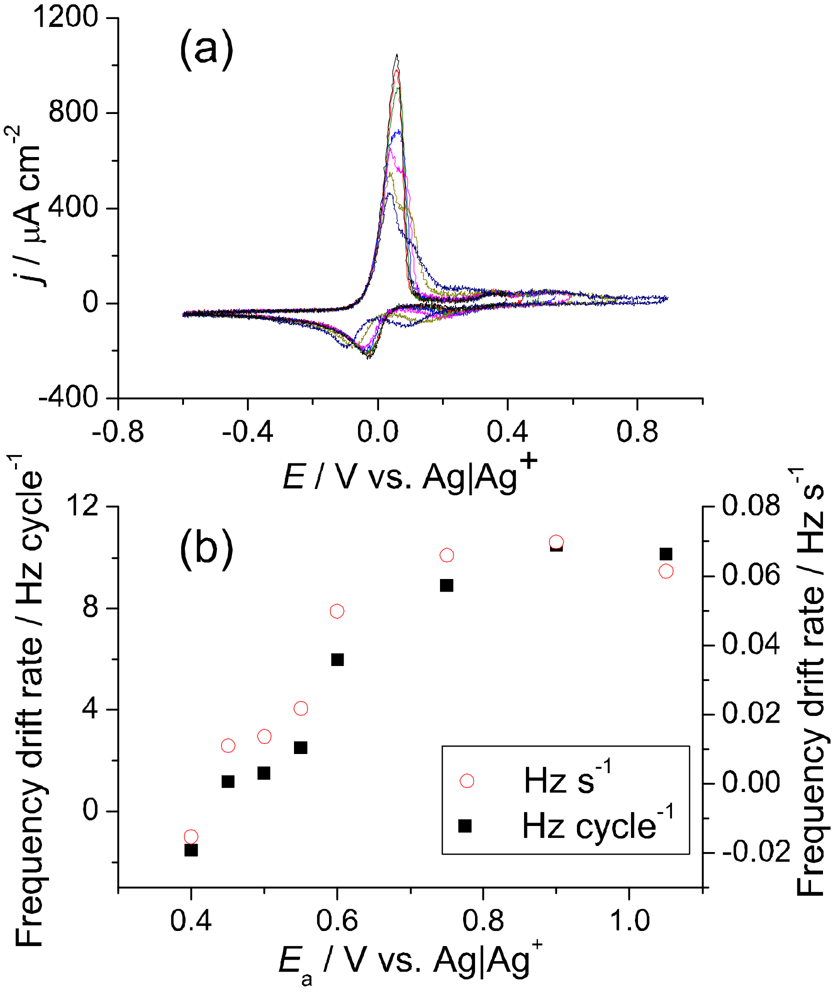

Figure 5.11: The Pt cyclic voltammograms in 1 mM $AgClO_4$ solution with different anodic reversal potentials (E_a). Sweep rate 50 mV s^{-1}.

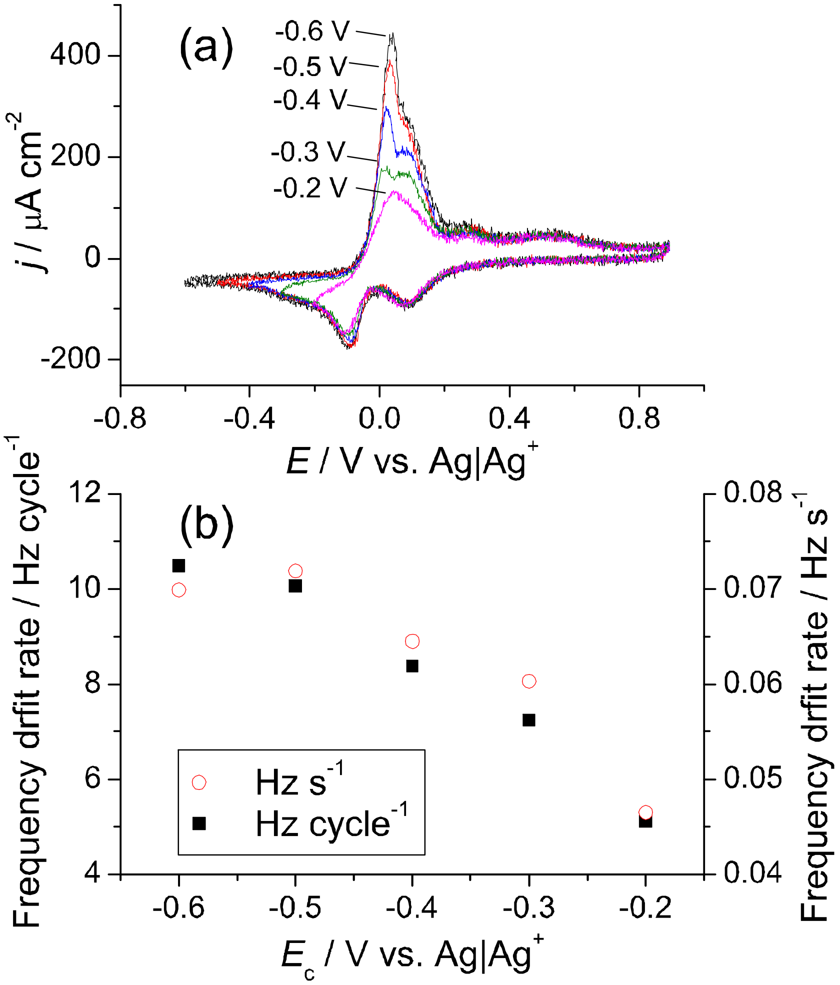

Figure 5.12: The Pt cyclic voltammograms in 1 mM $AgClO_4$ solution with different cathodic potential limits (E_c), 20 mV s^{-1}.

the slow Pt-Ag place exchange and alloy formation, i.e., the time gap between the onset of UPD and the anodic peak a3 is greatly decreased when E_c is decreased by 0.4 V from the initial –0.6 V. This results in a decreased frequency drift rate and Pt dissolution rate. Given a growth time of 1.5 min at a sweep rate of 20 mV s^{-1} and E_c = 0.6 V, it is very likely that the formation of the stable Pt-Ag alloy requires at least a few minutes under our experimental conditions, close to Vaskevich's results [104].

5.6.2 Sweep rate dependence

An alternative way to investigate the time dependence of Pt-Ag alloy formation and its effect on Pt dissolution is by examining the frequency drift rates at different sweep rates. The recorded voltammograms and frequency drift rates at sweep rates from 5 mV s^{-1} to 500 mV s^{-1} are shown in Fig 5.13. The frequency drift rate (Hz $cycle^{-1}$) at sweep rates from 8.33 mV s^{-1} to 100 mV s^{-1} doesn't show a clear trend with increasing sweep rate, but remains approximately the same at ca. 8.0 Hz $cycle^{-1}$. At sweep rates higher than 100 mV s^{-1}, the frequency drift rate (Hz $cycle^{-1}$) drops steadily with increasing sweep rate. The charge and frequency analysis for anodic peak a3 in Section 5.2 shows that fewer monolayers of Ag are underpotentially deposited at higher sweep rate (see Table 5.1), while higher sweep rates also means less time is available for Pt-Ag alloy growth. Both these factors lead to the decreased Pt dissolution rate at higher sweep rate.

5.6.3 Temperature dependence

The platinum dissolution was also examined at different system temperatures, from 21.3 °C to 49.5 °C (see Fig. 5.14). At elevated temperatures, the UPD current is significantly increased and the peak potential shifts positively. The OPD is less affected by temperature: the OPD peak current remains unchanged and the peak

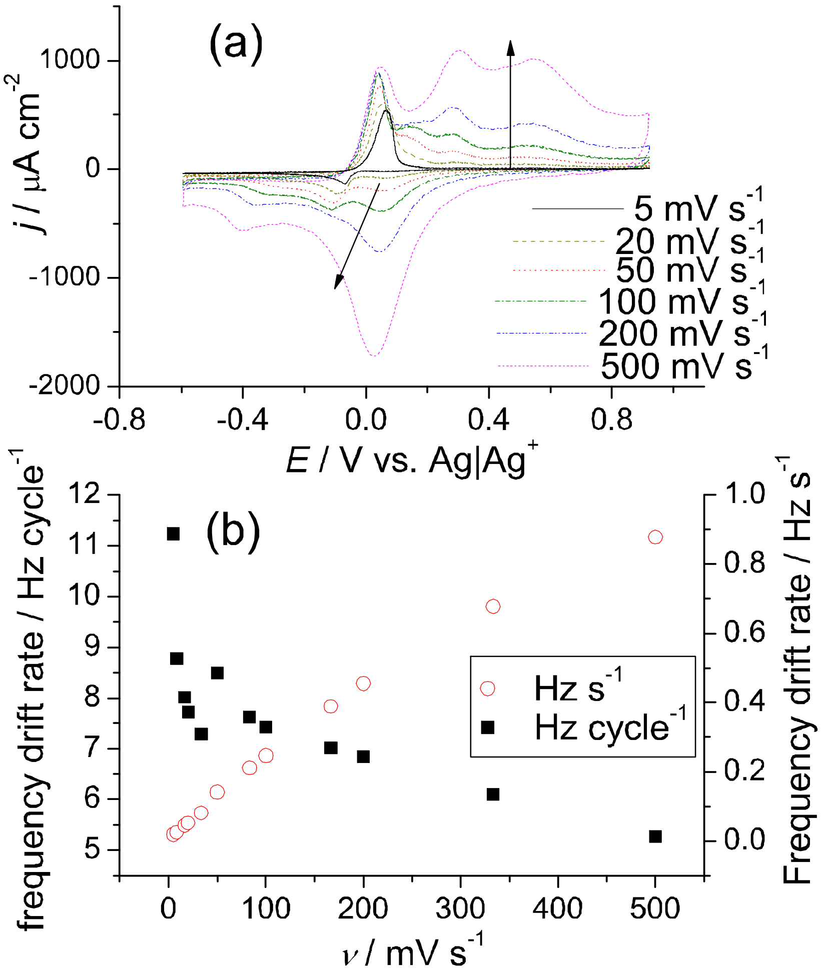

Figure 5.13: The Pt cyclic voltammograms in 1 mM $AgClO_4$ solution at different sweep rates from 5 to 500 mV s^{-1} (arrow refers to increase in sweep rate). Potential range –0.6 V to 0.9 V vs. Ag|Ag$^+$.

potential shifts slightly positive. The peak current for the anodic stripping peak a1 increases, and meanwhile, the stripping peak a2 is significantly suppressed.

The frequency drift rate shows a parabolic dependence on temperature, and a maximum frequency drift rate was observed at ca. 40 °C. The frequency drift rate slightly decreases at $T > 40.0$ °C, but the reason for this is not clear.

5.7 Discussion

ICP-MS results showed that the Pt working electrode has little dissolution (0.0011 monolayer cycle^{-1}) when cycling at full potential range from 0.05 V to 1.5 V vs. RHE in 0.5 M $HClO_4$. Even successive cycling for 12 h only resulted in +286 Hz of total frequency drift which equals a total of ca. 3.7 monolayers of Pt or 0.0013 monolayer cycle^{-1}. In the literature, it has been observed that potential cycling to high anodic potential limit ($E_\mathrm{a} > 1.6$ V vs. RHE) followed by a fast reduction cycle produces a Pt concentration in solution detectable by the stannous chloride test [87]. Dissolution at high anodic potentials is reasonable since higher Pt-O coordination numbers and a higher degree of place-exchange effectively weakens the bonding between metallic Pt atoms and Pt atoms in an oxide film. However, significant Pt dissolution under mild conditions ($E_\mathrm{a} < 1.6$ V vs. RHE) has also been reported. Johnson et al. [88] performed the CV experiments between 0.45 and 1.45 V vs. RHE at sweep rate 100 mV s^{-1} and detected soluble Pt species in solution equivalent to 0.011 monolayer cycle^{-1} in 1 M H_2SO_4 and 0.008 monolayer cycle^{-1} in 0.1 M $HClO_4$ (10 times higher than our dissolution rate). Rand et al. [89] found a Pt dissolution rate close to (15% higher) Johnson's results, when cycling between 0.41 V and 1.46 V vs. RHE at 40 mV s^{-1} in 1 M H_2SO_4. Recently Yadav [108] used a 65 nm-thick electrochemically deposited Pt electrode, and observed a dissolution rate of 0.006 ML cycle^{-1} when cycling between 0.0 and 1.4 V vs. RHE. These authors used Pt electrodes with roughness factors of 1-3 or higher than 10 and performed extensive cycling to study

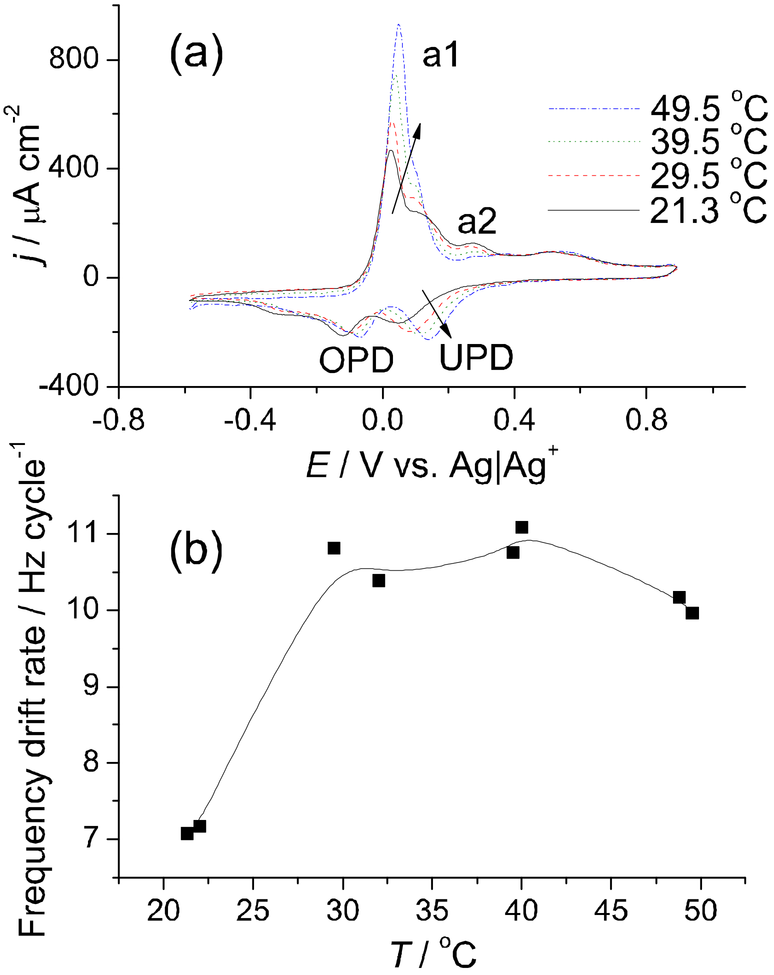

Figure 5.14: The Pt cyclic voltammograms in 1 mM $AgClO_4$ solution at different system temperatures (arrrow refers to increase in temperature). Potential range –0.6 V to 0.9 V vs. Ag|Ag^+. sweep rate 50 mV s^{-1},

the roughness change and Pt dissolution. Our sputter-deposited Pt has a surface with a mirror finish, and both AFM and hydrogen adsorption data give a very small roughness factor of only 1.1−1.2, which probably explains the lower dissolution in our case. The smoother surface is more inert to acid during potential cycling and leads to smaller changes in surface roughness and less Pt dissolution. There may be a chance for faster Pt dissolution when the surface becomes sufficiently rough after continuous cycling for a very long time (t >12 h), but we did not find this effect on the time scales we observed.

Addition of 1 mM Ag^+ into 0.5 M $HClO_4$ initiated an immediate large frequency drift of 8.3 Hz $cycle^{-1}$ or 0.11 ML of Pt per cycle, which is 100 times faster than the control experiments in $HClO_4$. It is evident that the Ag deposition/stripping in the low potential region ($E < 0.3$ V vs. $Ag|Ag^+$) is mixed with Pt oxide formation/reduction in the high potential region (E > 0.7 V vs. $Ag|Ag^+$). However, these observed reactions by themselves can't contribute to the high rates of Pt dissolution. Therefore the Ag deposition and stripping must play a kind of electrocatalytic role in activating the Pt dissolution. During the Ag UPD deposition, the first monolayer of Ag undergoes a slow place-exchange with surface Pt atoms to form a well defined Pt-Ag surface alloy with a thickness of ca. two monolayers [104,109,110]. This Pt-Ag surface alloy has been identified by STM [111] and Auger spectroscopy [101], and has been found on both single and polycrystalline Pt surfaces. The ratio between the Pt and Ag atoms could vary, and a typical composition of $Ag_{80}Pt_{20}$ was found by Batzil [102]. At the end of the anodic cycle, the alloyed Ag will be stripped, leaving some Pt atoms at higher energy kink or adatom sites. Repetitive UPD and stripping alters the smooth surface and leads to microscopic surface roughening. These higher energy sites lead to higher Pt dissolution rates. A diagram describing such processes is shown in Fig. 5.15. The large amount of Pt dissolution implies a high yield of Pt-Ag surface alloy during UPD to switch the Ag and Pt atoms, and brings the Pt atoms out of the Pt lattice. Such place-exchange process is very similar to

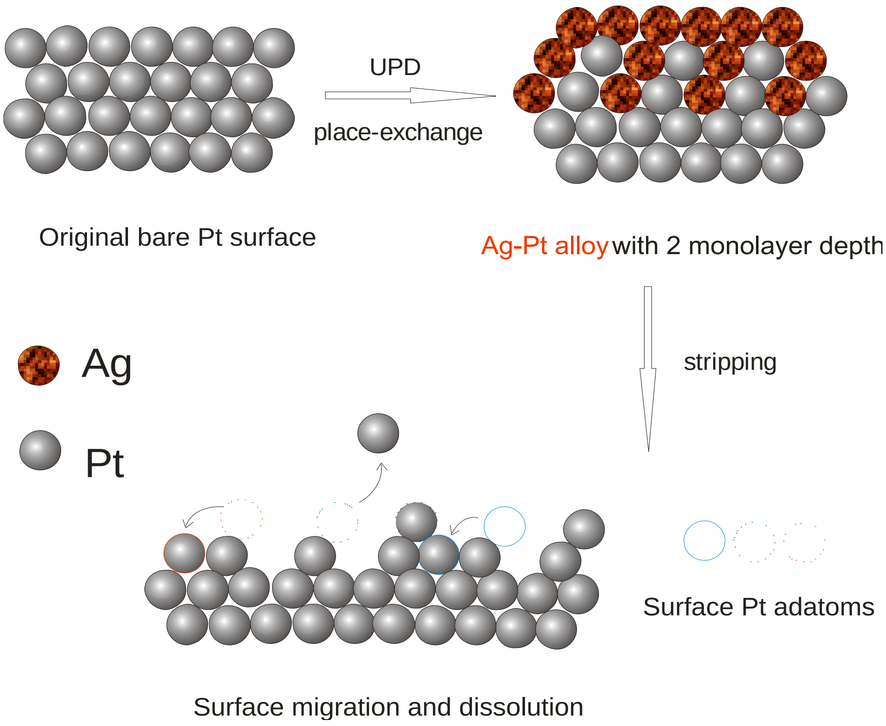

Figure 5.15: Schematic of the sequence from Pt-Ag alloy formation to stripping of the alloy, which results in Pt surface roughening and dissolution.

the place-exchange of Pt and O atoms during Pt oxidation. During the reduction of the place-exchanged "Pt-O" 3-D structure in $HClO_4$ solutions, the Pt(II) species are reduced to Pt atoms and remain on the surface, with some in high energy sites. Dissolution could occur from these sites or directly from the film. However, the observed dissolution rate is much less than with Ag present, and therefore promotion by Ag must require something more than just Pt atoms in high energy sites. During the anodic stripping of place-exchanged Pt-Ag alloy, the last Ag monolayers may be stripped partially in the form of soluble Pt-Ag cluster species, resulting in accelerated dissolution of surface Pt into the solution. Łukaszewski et al. [112] investigated the dissolution of noble metals (Pd, Pt, Rh) and their alloys during potential cycling by EQCM, and found that the Pt surface alloyed with a less noble metal (e.g., Pd) could dissolve into 0.5 M H_2SO_4 to a much greater extent than pure Pt metal.

The above mechanism implies that Pt dissolution and roughening occur simultaneously. AFM topography clearly showed the surface roughening after extensive cycling (Fig. 5.10) under the conditions where Pt dissolution occurs.

5.8 Conclusions

Successive potential cycling in pure $HClO_4$ solution resulted in Pt dissolution from the electrode surface only to a very small extent, 0.0011 monolayer cycle^{-1}. The deposition and stripping of Ag multilayers under the same electrochemical conditions caused Pt dissolution to a much greater extent, 0.11 monolayer cycle^{-1}. The dissolution of Pt during Ag deposition and stripping requires a minimum anodic potential limit of 0.43 V vs. $Ag|Ag^+$ and the rate of dissolution is slightly affected by the cathodic potential limit. The rate of dissolution decreases with increasing sweep rate and increases with increasing system temperature up to 40 °C. The enhanced extent of Pt dissolution arises because of the partial dissolution of the Pt-Ag surface alloy during the anodic stripping cycle. The formation of the Pt-Ag surface alloy during underpotential deposition of Ag and its growth during the overpotential deposition are the critical processes that lead to Pt dissolution.

Chapter 6

Conclusions

In this thesis, the potential of EQCM as a important technique to elucidate mechanisms of electrochemical reactions on the Pt surfaces was explored. The EQCM is powerful mainly because it allows addition of one more parameter (mass) to the list of parameters monitored in a standard electrochemical experiment (e.g., current, charge). This helps identify and classify the events taking place at the electrode with greater certainty and understanding. Potential cycling in H_2SO_4 solution resulted in surface reactions involving light-weight species (e.g. H_2O, H^+) and a small mass change was induced. The EQCM was still able to be used to study these species under such challenging conditions. In the case of Pt dissolution, the EQCM was capable of direct monitoring of the amount of Pt dissolved from electrode surface with high confidence. We found good stability and accuracy of our EQCM system in the frequency measurements.

H_2 gas is a good candidate molecule to probe the oxide film growth in the initial stage of Pt oxidation. The patched Pt surface by oxide film resulted in decreased reaction rate of H_2 oxidation, and the H_2 oxidation was completely inhibited when the Pt surface is covered by a full monolayer of oxide film. The purpose of using such probe molecules to monitor the oxide film coverage change during the whole initial stage of Pt oxidation was to identify clearly the starting and finishing point of the growth of a full oxide monolayer. We observed an onset potential for oxide formation at 0.85 V, where the net H_2 oxidation current (j_{ox}) begins to drop, and a finishing point at 1.15 V which marks the complete formation of a full oxide monolayer, where j_{ox} approaches a negligible residual current. Our methodology allows usage of other potential probe molecules such as O_2, and the experimental procedures can be performed under controlled-convection conditions, where improved j_{ox} profiles are observed.

The EQCM frequency analysis was performed for identification of the initial oxidation species, by correlating the frequency and charge density. Our results simply showed that the initial oxidation species was most likely anhydrous Pt_2O, as has been suggested by a few authors. The frequency analysis for the early stage of oxidation could be greatly complicated when anion adsorption is considered. A more detailed consideration of this effect is a topic for future research work.

The Pt dissolution with Ag present is significantly higher than without Ag present (where the Pt oxidation and reduction accounts only for a small extent of Pt dissolution). Examination of the potential, sweep rate and temperature dependence of Pt dissolution leads to the conclusion that the Pt-Ag surface alloy formed by slow place exchange of Pt and Ag atoms is required for the enhanced extent of Pt dissolution. The Pt atoms were brought out of their bulk lattice sites by place exchange and were left at high energy sites upon complete stripping of the deposited Ag layers, and these processes contribute to the higher rate of Pt dissolution. However, the observed dissolution rate at 0.11 ML cycle^{-1} appears to be mainly contributed from the direct dissolution of Pt in the form of an Ag-Pt species, since the alloy has a similar solubility as pure Ag metal.

This thesis also explored some new fields which require further work. The method of directly probing of oxide film formation with H_2 candidate molecule could be improved by using a more accurate determination of the net oxidation current by considering the interaction of H_2 with other surface species. Alternative probe molecules could be selected and carefully tested. Frequency analysis of early stage of Pt oxidation could be done in more detail by considering the anion adsorption. The formation of the Pt-Ag alloy which plays the key role for enhanced Pt dissolution could be further studied, and the structure and composition of this alloy needs to be identified.

References

[1] G. Sauerbrey, *Zeitschrift fur Physik*, 1959, **155**, 206.

[2] S. Bruckenstein and M. Shay, *Electrochimica Acta*, 1985, **30**, 1295.

[3] K. K. Kanazawa and J. G. Gordon, *Analytica Chimica Acta*, 1985, **175**, 99.

[4] S. Gilman in *Electroanalytical Chemistry*, ed. A. J. Bard, Vol. 2; Marcel Dekker, New York, 1967; p. 111.

[5] R. Woods in *Electroanalytical Chemistry*, ed. A. J. Bard, Vol. 9; Marcel Dekker, New York, 1976; p. 1.

[6] B. E. Conway, *Progress in Surface Science*, 1995, **49**, 331.

[7] C. A. Jeffrey *Electrodeposition and Characterisation of Thin Films and Nanostructures Based on Bismuth, Silver and Iodine,* PhD thesis, University of Victoria, 2004.

[8] C. A. Jeffrey, W. M. Storr, and D. A. Harrington, *Journal of Electroanalytical Chemistry*, 2004, **569**, 61.

[9] A. J. Bard and L. R. Faulkner, *Electrochemical Methods: Fundamentals and Applications*, John Wiley and Sons Inc., New York, 1980.

[10] J. Hlavay and G. G. Guilbault, *Analytical Chemistry*, 1977, **49**, 1890.

[11] J. F. Alder and J. J. McCallum, *Analyst*, 1983, **108**, 1169.

[12] T. Nomura and M. Iijima, *Analytica Chimica Acta*, 1981, **131**, 97.

[13] W. P. Mason, W. O. Baker, H. J. McSkimin, and J. H. Heiss, *Physical Review*, 1949, **75**, 936.

[14] A. P. M. Glassford, *Journal of Vacuum Science and Technology*, 1978, **15**, 1836.

[15] V. Mecea and R. V. Bucur, *Thin Solid Films*, 1979, **60**, 73.

[16] R. A. Crane and G. Fischer, *Journal of Physics D*, 1979, **12**, 2019.

[17] G. Hayward, *Analytica Chimica Acta*, 1992, **264**, 23.

[18] D. M. Soares, M. A. Tenan, and S. Wasle, *Electrochimica Acta*, 1998, **44**, 263.

[19] J. P. Valentin, G. Theobald, and J. J. Gagnepain, *Journal of Applied Physics*, 1985, **58**, 1388.

[20] D. P. R. Raudonis and V. Daujotis, *Journal of Electroanalytical Chemistry*, 1993, **358**, 351.

[21] M. C. Santos, D. W. Miwa, and S. A. S. Machado, *Electrochemistry Communications*, 2000, **2**, 692.

[22] G. Zilberman, V. Tsionsky, and E. Gileadi, *Electrochimica Acta*, 2000, **45**, 3473.

[23] W. Lee, H. S. White, and M. D. Ward, *Analytical Chemistry*, 1993, **65**, 3232.

[24] R. Schumacher, G. Borges, and K. K. Kanazawa, *Surface Science*, 1985, **163**, L621.

[25] R. Schumacher, *Angewandte Chemie International Edition in English*, 1990, **29**, 329.

[26] R. Beck, U. Pittermann, and K. G. Weil, *Journal of the Electrochemical Society*, 1992, **139**, 453.

[27] M. Yang and M. Thompson, *Langmuir*, 1993, **9**, 1990.

[28] S. J. Martin, G. C. Frye, A. J. Ricco, and S. D. Senturia, *Analytical Chemistry*, 1993, **65**, 2910.

[29] M. Urbakh and L. Daikhin, *Langmuir*, 1994, **10**, 2836.

[30] M. Urbakh and L. Daikhin, *Physical Review B*, 1994, **49**, 4866.

[31] L. Daikhin and M. Urbakh, *Langmuir*, 1996, **12**, 6354.

[32] L. Daikhin, E. Gileadi, G. Katz, V. Tsionsky, M. Urbakh, and D. Zagidulin, *Analytical Chemistry*, 2002, **74**, 554.

[33] D. M. Ullevig, J. F. Evans, and M. G. Albrecht, *Analytical Chemistry*, 1982, **54**, 2341.

[34] M. D. Ward and E. J. Delawski, *Analytical Chemistry*, 1991, **63**, 886.

[35] S. J. Martin, *Faraday Discussions*, 1997, **107**, 463.

[36] M. Thompson, A. Kipling, W. C. Duncan-Hewitt, L. V. Rajakovic, and B. A. Cavic-Vlasak, *Analyst*, 1991, **116**, 881.

[37] B. Du, I. Goubaidoulline, and D. Johannsmann, *Langmuir*, 2004, **20**, 10617.

[38] L. Daikhin, E. Gileadi, V. Tsionsky, M. Urbakh, and G. Zilberman, *Electrochimica Acta*, 2000, **45**, 3615.

[39] B. A. Cavic, F. L. Chu, L. M. Furtado, S. Ghafouri, G. L. Harward, D. P. Mack, M. E. Mcgovern, H. Su, and M. Thompson, *Faraday Discussions*, 1997, **107**, 159.

[40] W. C. Duncan-Hewitt and M. Thompson, *Analytical Chemistry*, 1992, **64**, 94.

[41] G. McHale and M. I. Newton, *Journal of Applied Physics*, 2004, **95**, 373.

[42] L. Bouzidi, S. S. Narine, K. G. Stefanov, and A. J. Slavin, *Review of Scientific Instruments*, 2003, **74**, 3039.

[43] C. Gabrielli, M. Keddam, and R. Torresi, *Journal of the Electrochemical Society*, 1991, **138**, 2657.

[44] G. Vatankhah, J. Lessard, G. Jerkiewicz, A. Zolfaghari, and B. E. Conway, *Electrochimica Acta*, 2003, **48**, 1613.

[45] B. E. Conway, *Progress in Surface Science*, 1984, **16**, 1.

[46] M. E. Van der Geest, N. J. Dangerfield, and D. A. Harrington, *Journal of Electroanalytical Chemistry*, 1997, **420**, 89.

[47] C. A. Melendres, B. Beden, and G. A. Bowmaker, *Journal of Electroanalytical Chemistry*, 1995, **383**, 191.

[48] M. W. Breiter, *Journal of Electroanalytical Chemistry*, 1964, **7**, 38.

[49] B. E. Conway and S. Gottesfeld, *Journal of the Chemical Society Faraday Transactions I*, 1973, **69**, 1090.

[50] H. Angerstein-Kozlowska, B. E. Conway, and W. B. A. Sharp, *Journal of Electroanalytical Chemistry*, 1973, **43**, 9.

[51] B. E. Conway and J. Mozota, *Journal of the Chemical Society Faraday Transactions I*, 1982, **78**, 1717.

[52] M. Peuckert and H. Ibach, *Surface Science*, 1984, **136**, 319.

[53] J. B. Benziger, F. A. Pascal, and S. L. Bernasek, *Journal of Electroanalytical Chemistry*, 1986, **198**, 65.

[54] Y. Zhang, X. Gao, and M. J. Weaver, *Journal of Physical Chemistry*, 1993, **97**, 8656.

[55] H. Y. H. Chan, S. Zou, and M. J. Weaver, *Journal of Physical Chemistry B*, 1999, **103**, 11141.

[56] S. Zou, H. Y. H. Chan, C. T. Williams, and M. J. Weaver, *Langmuir*, 2000, **16**, 754.

[57] X. Li, D. Heryadi, and A. A. Gewirth, *Langmuir*, 2005, **21**, 9251.

[58] H. Angerstein-Kozlowska, B. E. Conway, and W. B. A. Sharp, *Journal of Electroanalytical Chemistry*, 1979, **43**, 9.

[59] D. L. Heyd and D. A. Harrington, *Journal of Electroanalytical Chemistry*, 1992, **335**, 19.

[60] D. A. Harrington, *Journal of Electroanalytical Chemistry*, 1997, **420**, 101.

[61] W. Nernst and E. Merriam, *Zeitschrift fur Physikalische Chemie*, 1905, **53**, 235.

[62] O. Sackur, *Zeitschrift fur Physikalische Chemie*, 1906, **54**, 641.

[63] M. W. Breiter, *Electrochimica Acta*, 1962, **7**, 601.

[64] V. I. Birss, M. Chang, and J. Segal, *Journal of Electroanalytical Chemistry*, 1993, **355**, 181.

[65] A. Zolfaghari, B. E. Conway, and G. Jerkiewicz, *Electrochimica Acta*, 2002, **47**, 1173.

[66] G. Jerkiewicz, G. Vatankhah, J. Lessard, M. P. Soriaga, and Y. S. Park, *Electrochimica Acta*, 2004, **49**, 1451.

[67] B. E. Conway, *Journal of Electroanalytical Chemistry*, 2002, **524**, 4.

[68] J. X. Wang, T. E. Springer, and R. R. Adzic, *Journal of the Electrochemical Society*, 2006, **153**, A1732.

[69] A. B. Anderson and T. V. Albu, *Journal of the Electrochemical Society*, 2000, **147**, 4229.

[70] C. R. Wilke and P. Chang, *AIChE Journal*, 1955, **1**, 264.

[71] D. R. Lide, *CRC Handbook of Chemistry and Physics*, CRC Press, Florida, 73 ed., 1992-1993.

[72] M. E. Gamboa-Aldeco, E. Herrero, P. S. Zelenay, and A. Wieckowski, *Journal of Electroanalytical Chemistry*, 1993, **348**, 451.

[73] W. Savich, S. Sun, J. Lipkowski, and A. Wieckowski, *Journal of Electroanalytical Chemistry*, 1995, **388**, 233.

[74] V. E. Kazarinov and N. A. Balashova, *Doklady Akademii Nauk SSSR*, 1964, **157**, 157.

[75] K. Shimazu and H. Kita, *Journal of Electroanalytical Chemistry*, 1992, **341**, 361.

[76] A. Frumkin and E. Aikasjan, *Doklady Akademii Nauk SSSR*, 1955, **100**, 315.

[77] A. N. Frumkin, *Journal of the Electrochemical Society*, 1960, **107**, 461.

[78] J. Bao and D. D. Macdonald, *Journal of Electroanalytical Chemistry*, 2007, **600**, 205.

[79] J. Tafel and B. Emmert, *Z. Phys. Chem*, 1905, **52**, 349.

[80] S. B. Brummer, *Journal of the Electrochemical Society*, 1965, **112**, 633.

[81] S. D. James, *Journal of the Electrochemical Society*, 1967, **114**, 111.

[82] P. Malachesky, R. Jasinski, and B. Burrows, *Journal of the Electrochemical Society*, 1967, **114**, 1104.

[83] M. W. Breiter, *Electrochimica Acta*, 1966, **11**, 905.

[84] S. Schuldiner and T. B. Warner, *Journal of the Electrochemical Society*, 1965, **112**, 212.

[85] R. Thacker and J. P. Hoare, *Journal of Electroanalytical Chemistry*, 1971, **30**, 1.

[86] H. A. Laitinen and C. G. Enke, *Journal of the Electrochemical Society*, 1960, **107**, 773.

[87] T. Biegler, *Journal of the Electrochemical Society*, 1969, **116**, 1131.

[88] D. C. Johnson, D. T. Napp, and S. Bruckenstein, *Electrochimica Acta*, 1970, **15**, 1493.

[89] D. A. J. Rand, *Journal of Electroanalytical Chemistry*, 1972, **35**, 209–218.

[90] D. F. Untereker and S. Bruckenstein, *Journal of the Electrochemical Society*, 1974, **121**, 360.

[91] K. I. Ota, S. Nishigori, and N. Kamiya, *Journal of Electroanalytical Chemistry*, 1988, **257**, 205.

[92] P. Bindra, S. J. Clouser, and E. Yeager, *Journal of the Electrochemical Society*, 1979, **126**, 1631.

[93] R. M. Darling and J. P. Meyers, *Journal of the Electrochemical Society*, 2003, **150**, A1523.

[94] V. Komanicky, K. C. Chang, A. Menzel, N. M. Markovic, H. You, X. Wang, and D. Myers, *Journal of the Electrochemical Society*, 2006, **153**, B446.

[95] H. You and Z. Nagy, *Physica B*, 1994, **198**, 187.

[96] K. Itaya, S. Sugawara, and K. Sashikata, *The Journal of Vacuum Science and Technology A*, 1990, **8**, 515.

[97] F. T. Wagner and P. N. Ross Jr, *Surface Science*, 1985, **160**, 305.

[98] R. C. Salvarezza, D. V. Vasquez Moll, M. C. Giordano, and A. J. Arvia, *Journal of Electroanalytical Chemistry*, 1986, **213**, 301.

[99] D. P. Sandoz, R. M. Peekema, H. Freund, and J. C. F. Morrison, *Journal of Electroanalytical Chemistry*, 1970, **24**, 165.

[100] D. C. Alonzo and B. R. Scharifker, *Journal of Electroanalytical Chemistry*, 1989, **274**, 167.

[101] P. Ocon, P. Herrasti, C. Palacio, M. E. Vela, R. C. Salvarezza, L. Vazquez, and A. J. Arvia, *Journal of Electroanalytical Chemistry*, 1993, **357**, 339.

[102] M. Batzill and B. E. Koel, *Surface Science*, 2004, **553**, 50.

[103] A. J. Arvia, M. E. Martins, and R. C. Salvarezza, *Electrochimica Acta*, 1996, **41**, 2441.

[104] A. Vaskevich, M. Rosenblum, and E. Gileadi, *Journal of Electroanalytical Chemistry*, 1995, **383**, 167.

[105] G. W. Tindall and S. Bruckenstein, *Electrochimica Acta*, 1971, **16**, 245.

[106] T. Chierchie, C. Mayer, K. Jutner, and W. J. Lorenz, *Journal of Electroanalytical Chemistry*, 1985, **191**, 401.

[107] C. P. Wilde, S. V. De Cliff, K. C. Hui, and D. J. L. Brett, *Electrochimica Acta*, 2000, **45**, 3649.

[108] A. P. Yadav, A. Nishikata, and T. Tsuru, *Electrochimica Acta*, 2007, **52**, 7444.

[109] A. Vaskevich, M. Rosenblum, and E. Gileadi, *Journal of Electroanalytical Chemistry*, 1996, **412**, 117.

[110] A. Vaskevich and E. Gileadi, *Journal of Electroanalytical Chemistry*, 1998, **442**, 147–150.

[111] M. Batzill and B. E. Koel, *Europhysics Letters*, 2003, **64**, 70.

[112] M. Łukaszewski and A. Czerwiński, *Journal of Electroanalytical Chemistry*, 2006, **589**, 38.